JETP Letters, Vol. 77, No. 3, 2003, pp. 121–122. Translated from Pis'ma v Zhurnal Éksperimental'noĭ i Teoreticheskoĭ Fiziki, Vol. 77, No. 3, 2003, pp. 147–148.

On the Kinetics of Anomalous Muonium in Silicon

I. G. Ivanter[1], E. P. Krasnoperov[1, *], B. A. Nikol'skiĭ[1], A. N. Ponomarev[1], V. N. Duginov[2], and U. Zimmermann[3]

[1] *Russian Research Centre Kurchatov Institute, pl. Akademika Kurchatova 1, Moscow, 123182 Russia*

**e-mail: kep@isssph.kiae.ru*

[2] *Joint Institute for Nuclear Research, Dubna, Moscow region, 141980 Russia*

[3] *Paul Scherrer Institut, CH-5232 Villigen PSI, Switzerland*

Received December 6, 2002

The spin relaxation rate of anomalous muonium in a longitudinal magnetic field was measured in a silicon single crystal. The results are treated as the diffusion of anomalous muonium in a silicon crystal. © *2003 MAIK "Nauka/Interperiodica".*

PACS numbers: 76.75.+i

In this work, the interactions of anomalous muonium Mu* were investigated in silicon at the temperature T = (150–175) K in a longitudinal magnetic field H = 3.1 kOe. A high-purity silicon single crystal (the number of impurities was $\leq 10^{12}$ cm^{-3}) whose [111] axis was oriented along the beam of longitudinally polarized muons with an accuracy of ~2° was used. The position of anomalous muonium in a silicon crystal was studied in a number of works (see references cited in [1]). It was shown that Mu* is localized on the body diagonal of a crystal between two silicon atoms, one of which is at the vertex of the basis cube of the crystal lattice and the other is shifted towards this diagonal by one-quarter of its length. The magnetic field $H\mu$ on the muon in anomalous muonium depends on the orientation of the silicon crystal and on the external magnetic field. According to [2], if the [111] axis is oriented along the external magnetic field H = 3.1 kOe, the muon is subjected to a local magnetic field $H\mu$ = 878 G that is the same for Mu* localized on the [–111], [1–11], and [–1–11] diagonals and to $H\mu$ = 2480 G for Mu* localized on the [111] diagonal. The longitudinal magnetic field $H\mu$ = 878 G on the first three diagonals is perpendicular to the external magnetic field H and gives rise to the characteristic precession of anomalous muonium. The longitudinal magnetic field $H\mu$ = 2480 G on the main [111] diagonal is directed along the external magnetic field H.

The experiment was carried out on the muon beam from the PSI accelerator (Villigen, Switzerland). The time dependence of muon polarization $P(t)$ was determined by scintillation counters that detected positrons emitted in the direction of the polarized muon beam from the $\mu^+ \longrightarrow e^+$ decay. The figure shows the experimental time dependence of muon polarization $P(t)_{\text{exp}}$ in anomalous muonium in the longitudinal magnetic field H = 3.1 kOe at temperature T = 170 K. As is seen in the figure, the $P(t)_{\text{exp}}$ dependence can be approximated by the following two processes: rapidly damped precession and slow depolarization of muon spin; i.e.,

$$P(t)_{\text{exp}} = a_1 e^{-\lambda_1 t}\cos\omega t + a_2 e^{-\lambda_2 t}. \qquad (1)$$

Here, the first term describes the damped precession of Mu* and the second term describes the exponential depolarization of muon spin. The frequency ω in Eq. (1) corresponds to the precession frequency of anomalous muonium in silicon. The experimentally determined parameters a_1, λ_1, a_2, and λ_2 are given in the table.

These features of the relaxation process $P(t)_{\text{exp}}$ (1) of anomalous muonium in silicon can be explained as fol-

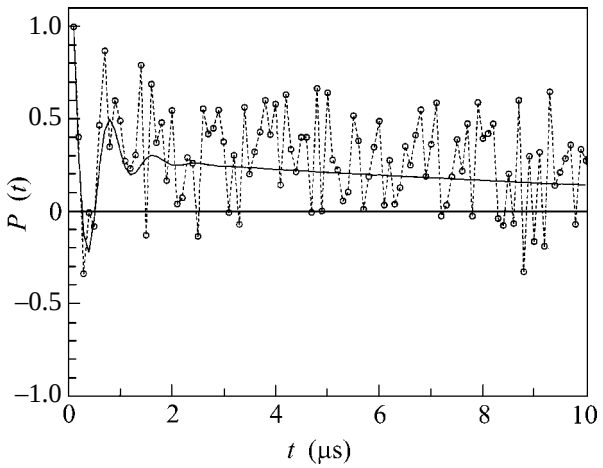

Time dependence of the polarization $P(t)$ of anomalous muonium in silicon in the longitudinal magnetic field H = 3.1 kOe at temperature T = 170 K. The smooth line is approximate dependence (1) normalized to $P(t = 0) = 1$.

Experimental parameters a_1, λ_1, a_2, and λ_2 in Eq. (1) at T = (150–175) K

T, K	a_1	λ_1, μs^{-1}	a_2	λ_2, μs^{-1}
150	0.84 (14)	5.8 (1.5)	0.18 (6)	0.8 (6)
160	0.65 (14)	6.5 (1.8)	0.24 (4)	1.4 (5)
165	0.77 (14)	9.4 (2.1)	0.20 (6)	0.5 (3)
170	0.90 (28)	21.7 (7.0)	0.22 (4)	0.7 (3)
175	0.67 (22)	14.4 (6.0)	0.37 (8)	0.6 (3)

lows. We assume that the rapid ($\lambda_1 \sim 10\ \mu s^{-1}$) decrease in the precession amplitude a_1 of anomalous muonium is caused by a certain incoherent excitation of Mu* with the conservation of muonium axial symmetry. This process does not affect the longitudinal (along the [111] axis) relaxation of Mu* localized on the [111] diagonal. We also treat the observed slow longitudinal spin relaxation of muon with $\lambda_2 \sim 1\ \mu s^{-1}$ as the process of diffusion jump of Mu* from the [111] diagonal to one of the [11–1], [1–11], and [1–1–1] diagonals followed by rapid depolarization. This interpretation agrees with the fact that the experimental ratio

$$(a_2/a_1)_{\text{exp}} = 0.30 \pm 0.08 \qquad (2)$$

coincides with the theoretical ratio $a_2/a_1 = 1/3$ that follows from the above model of Mu* relaxation on different diagonals of the silicon crystal lattice.

REFERENCES

1. B. D. Patterson, Rev. Mod. Phys. **60**, 69 (1988).
2. K. H. Chow, R. L. Lichti, R. F. Kieff, *et al.*, Phys. Rev. B **50**, 8918 (1994).

Translated by R. Tyapaev

JETP Letters, Vol. 77, No. 3, 2003, pp. 123–125. Translated from Pis'ma v Zhurnal Éksperimental'noĭ i Teoreticheskoĭ Fiziki, Vol. 77, No. 3, 2003, pp. 149–152.

Non-Liouvillian Carbon Nucleus Accumulation at the ITEP Storage Accelerator Facility

N. N. Alekseev, D. G. Koshkarev*, and B. Yu. Sharkov

Institute of Theoretical and Experimental Physics, ul. Bol'shaya Cheremushkinskaya 25, Moscow, 117259 Russia

** e-mail: Koshkarev@vitep1.itep.ru*

Received November 27, 2002; in final form, December 17, 2002

Physical start-up of the new heavy-ion storage accelerator facility has been successfully performed at the Institute of Theoretical and Experimental Physics. Carbon nuclei with an energy of 200 MeV/n are accumulated in the storage ring of the 10-GeV U-10 proton synchrotron, which is converted into an ion accumulator. The accumulation is accomplished using solid-target charge exchange of C^{4+} ions that are accelerated in the UK booster synchrotron. Thus, non-Liouvillian carbon nucleus accumulation is accomplished experimentally. Our immediate goal is to raise the amount of accumulated nuclei to 2×10^{12}, which corresponds to the possibilities of the available facility configuration. © *2003 MAIK "Nauka/Interperiodica".*

PACS numbers: 29.20.Dh; 29.25.Ni

1. The terawatt storage-ring project at the Institute of Theoretical and Experimental Physics (TWS-ITEP) [1] is aimed at designing technologies of intense high-power (~1 TW) ion-beam generation and developing, on this base, the scientific and technical principles of research in the fields of the fundamental physics of extreme state of matter, relativistic nuclear physics, and inertial thermonuclear fusion in medical physics.

The generation of a powerful heavy-ion beam encounters certain difficulties. The first is associated with the so-called Coulomb limit in circular storage accelerators. It strongly restricts the attainable ion-beam density in the space of canonical variables.

The Coulomb limit restricts the number N of ions in the chamber of a circular storage accelerator according to the formula

$$N \sim \varepsilon\beta\gamma^2 AZ^{-2}. \quad (1)$$

In Eq. (1), A is the ion mass in atomic units; Z is the ion-to-electron charge ratio; ε is the invariant beam emittance, i.e., the emittance measured in the canonical coordinate–momentum variables; β is the ion velocity in units of velocity of light; and γ is a relativistic factor. It follows from Eq. (1) that a high ion-beam density (i.e., a large $N:\varepsilon$ ratio) can be obtained only for a sufficiently large value of $\beta\gamma^2$, i.e., only for a high ion energy. Since the ion acceleration always starts with a low energy, the ions should be accumulated after they have reached the maximum possible energy in the given accelerator. The second limitation is associated with the principle of ion-beam density conservation in the space of canonical variables, i.e., with the so-called Liouville theorem. According to this theorem, the phase volume occupied by particles in the six-dimensional space of canonical variables is conserved in the course of acceleration and accumulation if dissipative forces are absent. Consequently, ion accumulation will inevitably expand the phase volume.

For some important applications, there is little sense in this method of accumulation, because only beams with high phase density are ordinarily needed for experimental purposes, e.g., for focusing on a small target. Therefore, ion accumulation makes practical sense if ε is conserved, i.e., only for so-called non-Liouvillian injection. Since the Liouville theorem holds only for an ensemble of indistinguishable objects, the Liouville theorem fails for the superposition of ion beams differing in ion charge or mass. Evidently, this distinction between ions must be eliminated after the ion beams have been superposed in the coordinate and momentum space. In the case of different charges, this can easily be done by passing beams through a thin charge-exchange target.

The idea of non-Liouvillian accumulation was put forward by Academician G.I. Butker in 1963, who proposed that proton multiturn injection can be accomplished using H^--ion-beam charge exchange into protons in a thin target placed in the synchrotron chamber [2]. This proposal has not gained wide acceptance, because the energy of protons injected in a synchrotron is rather low, whereas, as mentioned above, the Coulomb-limiting intensity in this case can easily be achieved by conventional injection methods. An attempt at applying this method to heavy-ion accumulation encounters one more problem, which is associated with the presence of a large number of electrons at the atomic shells of the ions of these elements. For this reason, passage through the charge-exchange target is inevitably accompanied by an appreciable intensity loss. In some publications [3, 4], it was suggested that

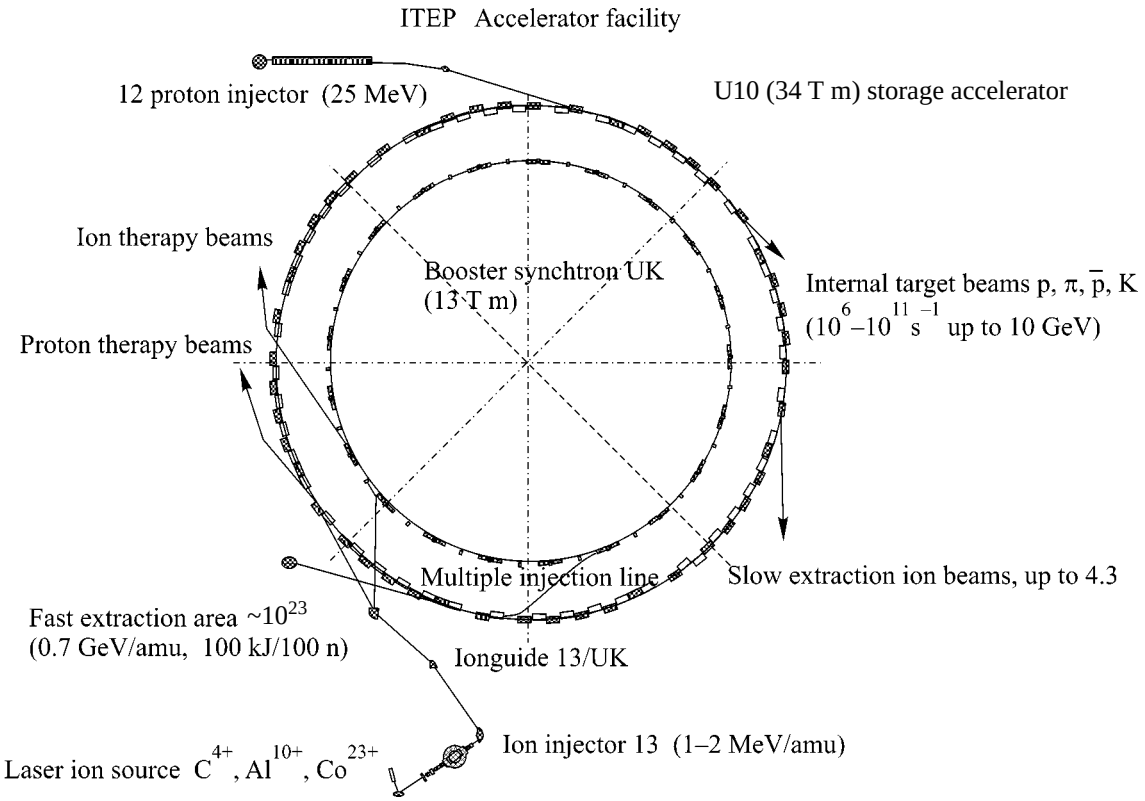

Fig. 1. General scheme of the TWS-ITEP accelerating-storage complex.

this problem can be obviated by using not a charge-exchange target but a powerful laser beam with the wavelength providing nonzero resonance charge-exchange cross section. This idea continues to be developed [5] but has not been implemented as yet. The reason is that the necessary powerful short-wavelength radiation can be generated only by complex and very costly free-electron lasers.

In the TWS project, it has become possible to go back to the idea of using a thin target for heavy-ion charge exchange, because only bare nuclei are accumulated in this project, with a sufficiently high energy for which the equilibrium ion charge becomes equal to the nuclear charge after passing through the target. At such a high energy, the probability of recombination electron capture in the target is negligibly small (10^{-3}) and even smaller, by a factor of 4×10^{-2}, if the beam geometry is taken into account; i.e., it is equal to 4×10^{-5}. Theoretically, this allows the intensity of the accumulated beam to be increased $\leq 10^4$ times as compared to the injected beam.

2. In the setup designed in the TWS project, an intense bare-nucleus beam with an energy up to 0.7 GeV/n is expected to accumulate in a storage ring remodeled from the annular magnet of the U-10 proton synchrotron.

An intense ion beam is accumulated in the following way. Incompletely stripped ions ($Z/A \sim 0.25$–0.45) with mass numbers $A \sim 60$ are produced in a laser source with an extraction potential of 50–100 kV. Next, the ions are accelerated in the I-3 linear injector to an energy of $Z \times 4$ MeV [6]. The total ion energy is achieved in the UK booster synchrotron. The accelerated ion beam is extracted from the UK after one turn and injected into the U-10 storage ring using the charge-exchange injection method [1, 7]. This process is repeated with a frequency of 1 Hz until the Coulomb limit is reached.

At present, the accumulation process is organized using a CO_2-laser source with a beam energy of ≈5 J. The rated beam-power level is expected to be obtained using a higher power laser with an energy of ~100 J [8]. Nevertheless, recent development of the laser source made it possible to improve its operation stability and raise the peak current of the C^{4+}-ion beam to 500 mA.

The maximal current of the C^{4+} ions at the I-3 injector output is as high as 5 mA for a peak beam current of 80 mA.

The UK booster synchrotron accelerates C^{4+} ions from an initial energy of 1.3 MeV/n to an energy of 300 MeV/n [9]. To accelerate ions, the acceleration frequency was tuned (15-fold) using two ferrite-filled cavities operating in tandem, one after another, with the

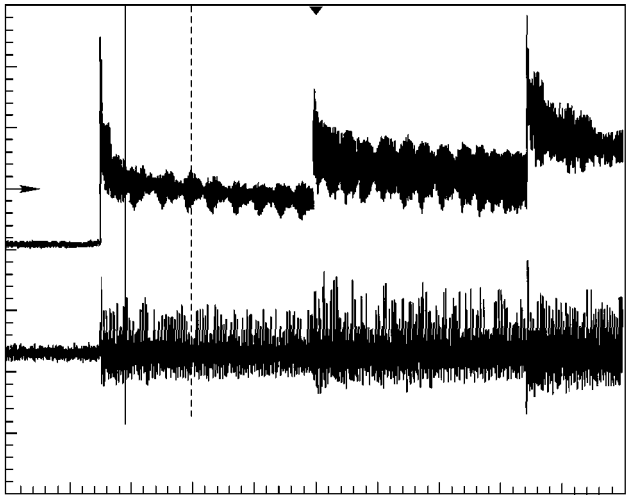

Fig. 2. Initial portion of the accumulation oscillogram of carbon ions with an energy of 200 MeV/n in the U-10 storage ring (top: beam intensity 5×10^8 ion/division; bottom: signal from the electrostatic transducer).

frequency tuning, respectively, in the ranges 0.6–2.2 and 2.2–10 MHz. Since the actuation of the accelerator in 2000, the intensity of the C^{4+}-ion beam at the UK output has increased more than an order of magnitude and has reached, at present, 2×10^9 particles per cycle.

The UK-accelerated beam is extracted after one turn for the subsequent charge-exchange injection into the U-10 storage ring (Fig. 1).

The number of ion passages through the charge-exchange target in the course of accumulation is minimized by focusing the circulating beam on the charge-exchange target only in the course of injection of a new portion of ions. This operation minimizes the perturbing action of the target on the accumulated beam (mylar charge-exchange target; target size 10×5 mm^2; target thickness 5 mg/cm^2).

3. The beam accumulation was adjusted in the presence of a microwave field with an amplitude of ≈1 kV. In this case, the injected beam was locked on from the tenth frequency multiplicity of the UK accelerating field to the second one of the U-10. The periodicity of the acceleration and injection cycles was 4.2 s. The trajectory of the injected beam was matched to the one-turn- deflected orbit of the circulating beam by tuning the crossing angle between the injection trajectory and the target, by varying the magnetic induction in the storage ring, by adjusting the target position in the storage chamber, and by the correction of the equilibrium orbit.

As a result of the multiple charge-exchange injection, $\geq 10^{10}$ carbon nuclei were accumulated in the U-10 storage ring (Fig. 2). Thus, the efficiency of the non-Liouvillian accumulation principle as a physical basis of the TWS-ITEP heavy-ion accumulation facility has been demonstrated experimentally using the charge-exchange injection of carbon ions.

4. In summary, the following steps in constructing the TWS-ITEP storage complex have been completed to date:

(1) multiply charged C^{4+} ions are obtained in a laser source;

(2) C^{4+} ions are accelerated in the I-3 linear injector;

(3) C^{4+} ions are accelerated in the UK booster synchrotron; and

(4) the ions are accumulated using the $C^{4+} \longrightarrow C^{6+}$ charge-exchange scheme in the U-10 storage ring up to a level of $\sim 10^{10}$ carbon nuclei.

Our immediate goal is to obtain the maximum attainable beam intensity for the available configuration of the complex.

REFERENCES

1. G. Koshkarev, N. N. Alekseev, and B. Yu. Sharkov, in *Proceedings of XV Meeting on Accelerators of Charged Particles* (Protvino, 1996), Vol. 2, p. 319.
2. G. I. Budker and G. I. Dimov, in *Proceedings of International Conference on Accelerators of Charged Particles, 1963* (Atomizdat, Moscow, 1964).
3. R. C. Arnold, D. G. Koshkarev, and B. Y. Sharkov, IEEE Trans. Nucl. Sci. **24**, 1428 (1977).
4. C. Rubbia, Nucl. Instrum. Methods Phys. Res. A **278**, 253 (1989).
5. I. Hofmann, Laser Part. Beams **8**, 527 (1990).
6. N. N. Alexeev, S. L. Bereznitsky, and V. I. Nikolaev, in *Proceedings of 7th European Particle Accelerator Conference, EPAC-2000* (Vienna, 2000), p. 1283.
7. B. Sharkov, G. Koshkarev, and M. D. Churazov, Nucl. Instrum. Methods Phys. Res. A **415** (1–2), 22 (1998).
8. B. Y. Sharkov, S. Kondrashov, and I. Roudskoy, Rev. Sci. Instrum. **69**, 1035 (1998).
9. N. N. Alekseev, V. N. Balanutsa, S. L. Bereznitskiĭ, *et al.*, in *Proceedings of XVII Meeting on Accelerators of Charged Particles* (Protvino, 2000), Vol. 2, p. 231.

Translated by V. Sakun

JETP Letters, Vol. 77, No. 3, 2003, pp. 126–131. Translated from Pis'ma v Zhurnal Éksperimental'noĭ i Teoreticheskoĭ Fiziki, Vol. 77, No. 3, 2003, pp. 153–158.

Andreev Conductance of a Ferromagnet–Superconductor Point Contact

B. P. Vodopyanov[1, *] and L. R. Tagirov[2]

[1] *Zavoĭskiĭ Physicotechnical Institute, Kazan Scientific Center, Russian Academy of Sciences, Kazan, 420029 Tatarstan, Russia*

**e-mail: vodop@kzn.ru*

[2] *Kazan State University, ul. Kremlevskaya 18, Kazan, 420008 Tatarstan, Russia*

Received December 10, 2002; in final form, December 30, 2002

Based on the boundary conditions derived for quasiclassical Green's functions, a theory of Andreev reflection in ferromagnet–superconductor point contacts is constructed. From a comparison with experimental data, the polarization of the conduction band was estimated for a number of ferromagnetic materials used in experiments on Andreev spectroscopy. © *2003 MAIK "Nauka/Interperiodica".*

PACS numbers: 74.50.+r; 74.81.-g

At low temperatures, an electric current flows through a normal metal/superconductor (N/S) interface as a result of Andreev reflection [1]. An electron is reflected from the N/S interface into a subband as a hole with the opposite spin, and the formed Cooper pair moves through the superconductor, transferring a charge 2*e*. The doubling of the conductance of a pure N/S microcontact was demonstrated in [2] (BTK) based on the solution of the Bogoliubov equations. In [3], attention was drawn to the fact that Andreev reflection in ferromagnet/superconductor (F/S) contacts is suppressed as the spin polarization of the ferromagnet conduction band grows. This is associated with the fact that the Andreev reflection efficiency is determined by the number of conducting channels in the subband with the lower value of the Fermi momentum. In [4–8], it was suggested that the suppression of Andreev reflection in F/S contacts be used for determining the spin polarization of the conduction band of ferromagnets (Andreev spectroscopy of ferromagnets). Experimental data were interpreted with the use of either general considerations that the spin-polarized component of the normal current does not pass through the superconductor [3–6] or the BTK equations semiphenomenologically adapted to F/S contacts [7, 8]. The BTK theory was generalized and applied to F/S point contacts in theoretical works [9–11]. The expressions obtained in those works for Andreev conductance were inconsistent with each other. Moreover, the results obtained in [9, 10] do not reproduce the equation for Andreev conductance at zero temperature, which, as we will show below, follows from physical considerations. Meanwhile, the number of experiments with the use of F/S contacts grows, which calls for an adequate theoretical understanding and description.

The goal of this work is to construct a consistent quasiclassical theory of Andreev reflection for heterogeneous structures with an F/S interface. For this purpose, we will derive quasiclassical equations of superconductivity for metals with a spin-split conduction band and obtain boundary conditions (BCs) for quasiclassical Green's functions (GFs) at an F/S interface. Next, we will compute the Andreev conductance of an F/S point contact and give an estimate for the polarization of conduction bands of ferromagnetic metals from a comparison with experiments on Andreev spectroscopy [4], which systematically differs from the estimates made in [4].

1. Equations of superconductivity and boundary conditions. The BCs for an F/S interface will be derived for quasiclassical temperature GFs. We will start from equations for equilibrium thermodynamic GFs in matrix form [12], taking into account the spin splitting of the conduction band

$$\left(i\varepsilon_n\tau_z + \frac{1}{2m}\frac{\partial^2}{\partial\mathbf{r}^2} + \hat{\Delta} + \hat{\mu} - U - \hat{\Sigma}\right)\hat{G}(\varepsilon_n, \mathbf{r}, \mathbf{r}') = \delta(\mathbf{r}-\mathbf{r}'). \quad (1)$$

Here, the GF $\hat{G}$ and the self-energy part $\hat{\Sigma}$ are matrices taking the form

$$\hat{G} = \begin{pmatrix} G_{\alpha a} & F_{\alpha -\alpha} \\ -\tilde{F}_{-\alpha\alpha} & \tilde{G}_{-\alpha -\alpha} \end{pmatrix}, \quad \hat{\Sigma} = \begin{pmatrix} \Sigma_{\alpha\alpha} & \Sigma_{\alpha -\alpha} \\ -\tilde{\Sigma}_{-\alpha\alpha} & \Sigma_{-\alpha -\alpha} \end{pmatrix}.$$

0021-3640/03/7703-0126$24.00

In addition,

$$\hat{\Delta} = \begin{pmatrix} 0 & \Delta \\ -\Delta^* & 0 \end{pmatrix}, \quad \hat{\mu} = \frac{1}{2m}\begin{pmatrix} p_{F\alpha}^2 & 0 \\ 0 & p_{F-\alpha}^2 \end{pmatrix},$$

τ_z is the Pauli matrix, $\varepsilon_n = (2n+1)\pi T$ is the Matsubara frequency, α is the spin index, Δ is the order parameter, $p_{F\alpha}$ is the Fermi momentum, U is the electron interaction energy with the electric potential, $\mathbf{r} = (x, \rho)$, and $\rho = (y, z)$. We assume that the F/S interface coincides with the plane $x = 0$. Passing in Eq. (1) to the Fourier representation with respect to the coordinate $\rho - \rho'$, we obtain the following equation for $\hat{G}(x, x') = \hat{G}(x, x', \rho_c, p_\parallel, \varepsilon_n)$ ($p_\parallel$ is the momentum in the contact plane, $\rho_c = (\rho + \rho')/2$; in what follows, the index c of ρ_c will be omitted):

$$\left(i\varepsilon_n\tau_z + \frac{1}{2m}\frac{\partial^2}{\partial x^2} + i\frac{\mathbf{v}_\parallel}{2}\frac{\partial}{\partial\rho} + \frac{\hat{p}_x^2}{2m} + \hat{\Delta} - U - \hat{\Sigma}\right)\hat{G}(x, x') = \delta(x - x'), \quad \frac{\hat{p}_x^2}{2m} = \hat{\mu} - \frac{p_\parallel^2}{2m}. \tag{2}$$

For heterogeneous structures with an N/S interface, the BCs for the quasiclassical equations of superconductivity were derived in [13]. For the $\hat{G}(z, z')$ function, we will use the Zaitsev representation while additionally taking into account the spin splitting of the conduction band. The quantities related to the metal on the left (right) side of the interface will be designated by indices 1 (2). For the sake of definiteness, we will assume that index 1 corresponds to the ferromagnet (F) and index 2, to the superconductor (S). Thus, for $x, x' < 0$

$$\hat{G} = e^{i\hat{p}_{x1}x}\hat{G}_{11}e^{-i\hat{p}_{x1}x'} + e^{-i\hat{p}_{x1}x}\hat{G}_{22}e^{i\hat{p}_{x1}x'} + e^{i\hat{p}_{x1}x}\hat{G}_{12}e^{i\hat{p}_{x1}x'} + e^{-i\hat{p}_{x1}x}\hat{G}_{21}e^{-i\hat{p}_{x1}x'}. \tag{3}$$

Here, $\hat{p}_{x1} = [\hat{p}_{F1}^2 - p_\parallel^2]^{1/2}$; for $x, x' > 0$, $\hat{p}_{x1}$ in Eq. (3) should be changed to $\hat{p}_{x2}$. Substituting Eq. (3) into Eq. (2) and neglecting the second derivative with respect to x, we obtain the equations for $\hat{G}_{kn}(x, x')$

$$\left(i\varepsilon_n\tau_z - i(-1)^k\hat{v}_{x1}\frac{\partial}{\partial x} + i\frac{\mathbf{v}_\parallel}{2}\frac{\partial}{\partial\rho} - U + \hat{\tilde{\Delta}}_k - \hat{\tilde{\Sigma}}_k\right)\hat{G}_{kn}(x, x') = 0, \quad x \neq x'. \tag{4}$$

Here, $\hat{\tilde{\Delta}}_k = e^{i(-1)^k\hat{p}_{x1}x}\hat{\Delta}e^{-i(-1)^k\hat{p}_{x1}x}$, and $\hat{\tilde{\Sigma}}_k$ is determined in the same way. For $x, x' > 0$, $\hat{v}_{x1}$ in Eq. (4) should be changed to $\hat{v}_{x2}$. The equation conjugate to Eq. (4) is derived similarly. Let us pass to functions $\hat{g} = \hat{g}(x, x', \hat{p}_{xj})$ and $\hat{\Upsilon} = \hat{\Upsilon}(x, x', \hat{p}_{xj})$, which depend on the sign of the variable $\hat{p}_{xj}$ and are continuous at the point $x = x'$

$$\hat{g} = \begin{cases} \hat{g}_> = 2i\sqrt{\hat{v}_{xj}}\hat{A}_1(x)\hat{G}_{11}(x, x')\hat{A}_1^*(x')\sqrt{\hat{v}_{xj}} \\ -\operatorname{sgn}(x - x'), \quad \hat{p}_{xj} > 0 \\ \hat{g}_< = 2i\sqrt{\hat{v}_{xj}}\hat{A}_2(x)\hat{G}_{22}(x, x')\hat{A}_2^*(x')\sqrt{\hat{v}_{xj}} \\ +\operatorname{sgn}(x - x'), \quad \hat{p}_{xj} < 0 \end{cases}$$

$$\hat{\Upsilon} = \begin{cases} \hat{\Upsilon}_> = 2i\sqrt{\hat{v}_{xj}}\hat{A}_1(x)\hat{G}_{12}(x, x')\hat{A}_2^*(x')\sqrt{\hat{v}_{xj}} \\ -\operatorname{sgn}(x - x'), \quad \hat{p}_{xj} > 0 \\ \hat{\Upsilon}_< = 2i\sqrt{\hat{v}_{xj}}\hat{A}_2(x)\hat{G}_{21}(x, x')\hat{A}_1^*(x')\sqrt{\hat{v}_{xj}} \\ +\operatorname{sgn}(x - x'), \quad \hat{p}_{xj} < 0. \end{cases} \tag{5}$$

In Eq. (5) $\hat{A}_k = e^{-i(-1)^k(p_{xj\alpha} - p_{xj(-\alpha)})\tau_z x/2}$. Let us substitute Eq. (5) into Eq. (4) and into the equation conjugate to Eq. (4). Finding the difference (for $n = k$) and the sum (for $n \neq k$) of the equations obtained, we will obtain the quasiclassical equations of superconductivity in metals with a split conduction band

$$\operatorname{sgn}(\hat{p}_{xj})\frac{\partial}{\partial x}\hat{g} + \frac{1}{2}\mathbf{v}_\parallel\frac{\partial}{\partial\rho}(\hat{v}_{xj}^{-1}\hat{g} + \hat{g}\hat{v}_{xj}^{-1}) + [\hat{K}, \hat{g}]_- = 0,$$

$$\operatorname{sgn}(\hat{p}_{xj})\frac{\partial}{\partial x}\hat{\Upsilon} + \frac{1}{2}\mathbf{v}_\parallel\frac{\partial}{\partial\rho}(\hat{v}_{xj}^{-1}\hat{\Upsilon} - \hat{\Upsilon}\hat{v}_{xj}^{-1}) + [\hat{K}, \hat{\Upsilon}]_+ = 0, \tag{6}$$

$$\hat{K} = -i\hat{v}_{xj}^{-1/2}(i\varepsilon_n\tau_z + \hat{\Delta} - \hat{\Sigma})\hat{v}_{xj}^{-1/2} - i(p_{xj\alpha} - p_{xj(-\alpha)})\tau_z/2,$$

$$[a, b]_\pm = ab \pm ba.$$

In the case of an F/S interface, as well as for an N/S interface, a system of quasiclassical equations arises. In addition to functions $\hat{g}$, functions $\hat{\Upsilon}$ appears, which describe waves reflected from the interface. The system of Eqs. (6) must be supplemented with BCs.

The interface is characterized by the transmission and reflection coefficients $\hat{D}$ and $\hat{R} = 1 - \hat{D}$, respectively. In this paper, we will not consider interactions that lead to the spin flip of an electron upon its passing the interface; therefore, matrices $\hat{D}$ and $\hat{R}$ have a diagonal form with respect to spin. They have the same structure as $\hat{\mu}$ (see Eq. (1)). Taking into account the explicit form of the GF given by Eq. (3) and joining the quasiclassical functions on both sides of the interface according to the procedure proposed by Zaitsev, we obtain, after simple but tedious calculations, the BCs for quasiclassical equations (6). For $p_\parallel \leq \min(p_{F\uparrow}, p_{F\downarrow}, p_S)$ (here, $p_{F\uparrow}$ and $p_{F\downarrow}$ are the Fermi momenta of spin subbands of the ferromagnet, and p_S is the Fermi

momentum of the superconductor), it is convenient to represent these conditions in the matrix form

$$\begin{pmatrix} \hat{a}^* & -\hat{b}^* \\ -\hat{b} & \hat{a} \end{pmatrix} (\check{V}_x^F)^{\frac{1}{2}} \begin{pmatrix} \hat{g}_>^F & \hat{\Upsilon}_>^F \\ \hat{\Upsilon}_<^F & \hat{g}_<^F \end{pmatrix} (\check{V}_x^F)^{-\frac{1}{2}} = (\check{V}_x^S)^{\frac{1}{2}} \begin{pmatrix} \hat{g}_>^S & \hat{\Upsilon}_>^S \\ \hat{\Upsilon}_<^S & \hat{g}_<^S \end{pmatrix} (\check{V}_x^S)^{-\frac{1}{2}} \begin{pmatrix} \hat{a}^* & \hat{b}^* \\ \hat{b} & \hat{a} \end{pmatrix}. \quad (7)$$

Here, $\hat{a} = \hat{d}^{-1}$, $\hat{b} = \hat{r}\hat{d}^{-1}$, $\hat{r}$ and $\hat{d}$ are the scattering amplitudes at the F/S interface [13], and the $\check{V}_x^{S(F)}$ matrix is the result of the direct product of a unit matrix by $\check{v}_x^{S(F)}$. Let us pass in Eq. (7) to functions $\hat{\tilde{g}}$ and $\hat{\tilde{\Upsilon}}$ using the equations

$$\begin{aligned} \hat{\tilde{g}}_>^F &= e^{i\frac{\hat{\vartheta}_r}{2}} \hat{g}_>^F e^{-i\frac{\hat{\vartheta}_r}{2}}, \quad \hat{\tilde{g}}_<^F = e^{-i\frac{\hat{\vartheta}_r}{2}} \hat{g}_<^F e^{i\frac{\hat{\vartheta}_r}{2}}, \\ \hat{\tilde{\Upsilon}}_>^F &= e^{i\frac{\hat{\vartheta}_r}{2}} \hat{\Upsilon}_>^F e^{i\frac{\hat{\vartheta}_r}{2}}, \quad \hat{\tilde{\Upsilon}}_<^F = e^{-i\frac{\hat{\vartheta}_r}{2}} \hat{\Upsilon}_<^F e^{-i\frac{\hat{\vartheta}_r}{2}}, \\ \hat{\tilde{g}}_>^S &= e^{i\hat{\vartheta}_{rd}} \hat{g}_>^S e^{-i\hat{\vartheta}_{rd}}, \quad \hat{\tilde{g}}_<^S = e^{-i\hat{\vartheta}_{rd}} \hat{g}_<^S e^{i\hat{\vartheta}_{rd}}, \\ \hat{\tilde{\Upsilon}}_>^S &= e^{i\hat{\vartheta}_{rd}} \hat{\Upsilon}_>^S e^{i\hat{\vartheta}_{rd}}, \quad \hat{\tilde{\Upsilon}}_<^S = e^{-i\hat{\vartheta}_{rd}} \hat{\Upsilon}_<^S e^{-i\hat{\vartheta}_{rd}}, \\ \hat{\vartheta}_{rd} &= \hat{\vartheta}_r/2 - \hat{\vartheta}_d, \end{aligned} \quad (8)$$

and next to $\hat{\tilde{g}}_{s(a)}$ and $\hat{\tilde{\Upsilon}}_{s(a)}$ matrices symmetric (s) and antisymmetric (a) with respect to variable p_{xj}

$$\hat{\tilde{g}}_{s(a)} = 1/2[\hat{\tilde{g}}_> \pm \hat{\tilde{g}}_<], \quad \hat{\tilde{\Upsilon}}_{s(a)} = 1/2[\hat{\tilde{\Upsilon}}_> \pm \hat{\tilde{\Upsilon}}_<].$$

In Eq. (8), $\hat{\vartheta}_r$ and $\hat{\vartheta}_d$ are the phases of the scattering amplitudes at the F/S interface. After that, the system of boundary conditions is readily solved with respect to $\hat{\tilde{\Upsilon}}_{s(a)}$ matrices and takes the following form:

$$\begin{aligned} (\hat{\tilde{g}}_a^S)_d &= (\hat{\tilde{g}}_a^F)_d, \quad (\hat{\tilde{\Upsilon}}_a^S)_d = (\hat{\tilde{\Upsilon}}_a^F)_d, \\ (\sqrt{\hat{R}_\alpha} - \sqrt{\hat{R}_{-\alpha}})(\hat{\tilde{\Upsilon}}_a^+)_n &= \alpha_3(\hat{\tilde{g}}_a^-)_n, \\ (\sqrt{\hat{R}_\alpha} - \sqrt{\hat{R}_{-\alpha}})(\hat{\tilde{\Upsilon}}_a^-)_n &= \alpha_4(\hat{\tilde{g}}_a^+)_n, \\ -\hat{\tilde{\Upsilon}}_s^- &= \sqrt{\hat{R}_\alpha}(\hat{\tilde{g}}_s^+)_d + \alpha_1(\hat{\tilde{g}}_s^+)_n, \\ -\hat{\tilde{\Upsilon}}_s^+ &= (\hat{R}_\alpha)^{-\frac{1}{2}}(\hat{\tilde{g}}_s^-)_d + \alpha_2(\hat{\tilde{g}}_s^-)_n, \end{aligned} \quad (9)$$

where $\hat{\tilde{g}}_{a(s)}^{\pm} = 1/2[\hat{\tilde{g}}_{a(s)}^S \pm \hat{\tilde{g}}_{a(s)}^F]$. The $\hat{\tilde{\Upsilon}}_{a(s)}^{\pm}$ functions are determined in the same way. Indices d and n designate the diagonal and off-diagonal parts of the matrix: $\hat{T}_{d(n)} = 1/2[\hat{T} \pm \tau_z \hat{T} \tau_z]$. The coefficients α_i equal

$$\alpha_{1(2)} = \frac{1 + \sqrt{R_\alpha R_{-\alpha}} \mp \sqrt{D_\alpha D_{-\alpha}}}{\sqrt{R_\alpha} + \sqrt{R_{-\alpha}}},$$

$$\alpha_{3(4)} = (1 - \sqrt{R_\alpha R_{-\alpha}} \pm \sqrt{D_\alpha D_{-\alpha}}).$$

If the interference of waves arriving from the neighboring interfaces can be neglected and $\hat{\tilde{g}}$ does not depend on ρ, a boundary condition containing only the $\hat{\tilde{g}}$ function can be obtained:

$$\begin{aligned} \hat{\tilde{g}}_a^+ \hat{f}_1 + \hat{f}_2 \hat{\tilde{g}}_a^+ + \hat{\tilde{g}}_a^- \hat{f}_3 + \hat{f}_4 \hat{\tilde{g}}_a^- &= \hat{f}_3 - \hat{f}_4, \\ \hat{\tilde{g}}_a^- \hat{f}_1 + \hat{f}_2 \hat{\tilde{g}}_a^- + \hat{\tilde{g}}_a^+ \hat{f}_3 + \hat{f}_4 \hat{\tilde{g}}_a^+ &= \hat{f}_1 - \hat{f}_2. \end{aligned} \quad (10)$$

The $\hat{f}_i$ matrices equal

$$\begin{aligned} \hat{f}_1 &= \hat{\tilde{\Upsilon}}_s^+ \hat{\tilde{g}}_s^- + \hat{\tilde{\Upsilon}}_s^- \hat{\tilde{g}}_s^+, \quad \hat{f}_2 = \hat{\tilde{g}}_s^+ \hat{\tilde{\Upsilon}}_s^- + \hat{\tilde{g}}_s^- \hat{\tilde{\Upsilon}}_s^+, \\ \hat{f}_3 &= \hat{\tilde{\Upsilon}}_s^+ \hat{\tilde{g}}_s^+ + \hat{\tilde{\Upsilon}}_s^- \hat{\tilde{g}}_s^-, \quad \hat{f}_4 = \hat{\tilde{g}}_s^+ \hat{\tilde{\Upsilon}}_s^+ + \hat{\tilde{g}}_s^- \hat{\tilde{\Upsilon}}_s^-. \end{aligned} \quad (11)$$

In this case, the system of BCs consists of Eqs. (10) and the first equation of Eqs. (9). Note that only the diagonal part of the $\hat{\tilde{g}}_a$ function is continuous at the F/S interface.

2. Andreev conductance of an F/S point contact. We will consider a hole of radius a in an impenetrable membrane as a model of a point contact. At zero temperature, the equation for Andreev conductance G_A can be written from the following physical considerations. Let us find the current in the ferromagnet at $p_{F\downarrow} < p_S$, $p_{F\uparrow}$. Then, in the case of specular reflection from the interface, $p_\parallel = p_{F\downarrow}\sin\vartheta_\downarrow = p_{F\uparrow}\sin\vartheta_\uparrow = p_S\sin\vartheta_S$, and the incidence angles of electrons that can be Andreev-reflected from the interface in the spin-up subband are determined from the relationship $p_{F\downarrow}\sin\vartheta_\downarrow = p_{F\uparrow}\sin\vartheta_\uparrow$ and depend only on the parameter $\delta = p_{F\downarrow}/p_{F\uparrow}$. Electrons incident at angles that do not fulfill this equation will undergo total internal reflection. The problem becomes equivalent to the problem of finding the conductance of a point contact of normal metals with different Fermi momenta (in this case, these are $p_{F\uparrow}$ and $p_{F\downarrow}$) when these metals are in direct contact. Using the known solution of this problem by Zaitsev (equation (38') in [13]), we find

$$G_A(T=0) = G_\downarrow \frac{8\delta(2+\delta)}{3(1+\delta)^2}, \quad G_\downarrow = \frac{e^2 p_{F\downarrow}^2 A}{4\pi^2}, \quad (12)$$

where A is the contact area. The equations for $G_A(T=0)$ obtained in [9, 10] do not coincide with this result. At $\delta = 1$, the Andreev conductance equals the doubled Sharvin conductance, which corresponds to the doubling of conductance as a result of Andreev reflection.

Let us now find an equation for the Andreev conductance in the case of arbitrary transmission coefficients. We will start with the equation for current I in the linear approximation with respect to electric field $\mathbf{E} = (E_x, 0, 0)$. The current will be calculated on the ferromagnet side at $x \longrightarrow 0$

$$I_x = \frac{e^2}{2m^2}\lim_{\mathbf{r}'\to\mathbf{r}}\left(\frac{\partial}{\partial x}-\frac{\partial}{\partial x'}\right)\mathrm{Tr}\tau_z\int_{-\infty}^{\infty}\frac{d\varepsilon}{4\pi T\cosh^2\dfrac{\varepsilon}{2T}} \quad (13)$$

$$\times\int d\mathbf{r}_1\hat{G}^R(\varepsilon,\mathbf{r},\mathbf{r}_1)E_x(\mathbf{r}_1)\tau_z\frac{\partial}{\partial x_1}\hat{G}^A(\varepsilon,\mathbf{r}_1,\mathbf{r}').$$

Here, $\hat{G}^{R(A)}$ is the retarded (advanced) GF, which is obtained from the temperature GFs (Eqs. (1), (3)) by substituting $\varepsilon \pm i\delta$ for $i\varepsilon_n$. Let us substitute representations given by Eqs. (3) and (5) into Eq. (13). After performing the Fourier transform with respect to the $\rho - \rho'$ coordinate, we will obtain the following equation for the ballistic conductance $G_{F/S}$ of an F/S point contact:

$$G_{F/S} = \frac{e^2A}{16\pi}\mathrm{Tr}\tau_z\int_{-\infty}^{\infty}\frac{d\varepsilon}{\cosh^2\dfrac{\varepsilon}{2T}}\int\frac{d\mathbf{p}_\parallel}{(2\pi)^2} \quad (14)$$

$$\times[1-\hat{g}_c^R\tau_z\hat{g}_c^A-\hat{g}_a^R\tau_z\hat{g}_a^A+\hat{\Upsilon}_c^R\tau_z\hat{\Upsilon}_c^A-\hat{\Upsilon}_a^R\tau_z\hat{\Upsilon}_a^A].$$

Now, we must solve the first of Eqs. (6) with the BCs given by Eq. (10). When $\hat{g}$ is independent of ρ, the solution to Eq. (6) takes the form

$$\hat{g}_j = e^{-\mathrm{sgn}(\hat{p}_{xj})\hat{K}x}\hat{C}_j(\mathbf{p}_{Fj})e^{\mathrm{sgn}(\hat{p}_{xj})\hat{K}x}+\hat{C}_j. \quad (15)$$

Matrices $\hat{C}_j$ represent the values of the $\hat{g}_j$ GF at large distances from the F/S interface:

$$\hat{C}_2 = \begin{pmatrix} g & f \\ -f^* & -g \end{pmatrix} = \frac{1}{\sqrt{\varepsilon_n^2+|\Delta|^2}}\begin{pmatrix} \varepsilon_n & -i\Delta \\ i\Delta^* & -\varepsilon_n \end{pmatrix}. \quad (16)$$

In Eq. (15), $\hat{g}_1$ must tend to $\hat{C}_j = \tau_z\mathrm{sgn}(\varepsilon_n)$ at $x \longrightarrow -\infty$, and $\hat{g}_2$ must tend to $\hat{C}_2$ at $x \longrightarrow \infty$. Performing the matrix multiplication in Eq. (15), we find that these conditions are fulfilled if the following relationships are obeyed:

$$\hat{C}_j\hat{C}_j(\mathbf{p}_{Fj}) = -\hat{C}_j(\mathbf{p}_{Fj})\hat{C}_j = \mathrm{sgn}(p_{xj})(-1)^j\hat{C}_j(\mathbf{p}_{Fj}).$$

From these relationships, it follows that

$$\hat{g}_{sj} = \hat{C}_j + (-1)^j\hat{C}_j\hat{C}_{aj}, \quad \hat{g}_{aj} \equiv \hat{C}_{aj}. \quad (17)$$

Passing in Eq. (17) to functions $\hat{g}_s^{\pm}$, substituting them into the system of BCs given by Eqs. (10), and solving it in the linear approximation with respect to $\hat{C}_a^{\pm}$ ($\hat{C}_a^{\pm} = 1/2[\hat{C}_a^S \pm \hat{C}_a^F]$), we find that

$$\hat{C}_a^{\pm} = -\frac{f(1-\sqrt{R_\alpha R_{-\alpha}}\pm\sqrt{D_\alpha D_{-\alpha}})}{2[1+\sqrt{R_\alpha R_{-\alpha}}+(1-\sqrt{R_\alpha R_{-\alpha}})g]}\tau_x. \quad (18)$$

Now, from Eq. (14) with regard to Eqs. (9) and (18), we find the Andreev conductance G_A of an F/S point contact:

$$G_A \equiv G_{F/S}(V=0) = e^2A\int_0^{\Delta}\frac{d\varepsilon}{4\pi T\cosh^2\left(\dfrac{\varepsilon}{2T}\right)} \quad (19)$$

$$\times\int\frac{d\mathbf{p}_\parallel}{(2\pi)^2}\frac{4|\Delta|^2D_\uparrow D_\downarrow}{(1+\sqrt{R_\uparrow R_\downarrow})^2|\Delta|^2-4\sqrt{R_\uparrow R_\downarrow}\varepsilon^2}.$$

It depends on the relationship between the Fermi momenta $p_{F\downarrow}$, $p_{F\uparrow}$, and p_S. Thus, at $p_{F\downarrow} < p_S < p_{F\uparrow}$, the equation for G_A takes the following form:

$$G_A = \frac{e^2p_{F\downarrow}^2A}{4\pi^2}\frac{|\Delta|}{T}\int_0^1\frac{dx}{\cosh^2\left(\dfrac{|\Delta|}{2T}x\right)} \quad (20)$$

$$\times\int_0^{\frac{\pi}{2}}d\vartheta_\downarrow\sin 2\vartheta_\downarrow\frac{D_\uparrow D_\downarrow}{(1+\sqrt{R_\uparrow R_\downarrow})^2-4\sqrt{R_\uparrow R_\downarrow}x^2}.$$

In the case of a nonmagnetic metal, where $D_\uparrow = D_\downarrow$, the equation for the Andreev conductance obtained in [13] follows from Eq. (20).

3. Discussion of experiments. The ratio of G_A to $G_{F/N}$, where $G_{F/N}$ is the conductance of an F/S contact in the normal state, was measured in [4–8]:

$$G_{F/N}(V=0) = \frac{e^2p_{F\downarrow}^2A}{8\pi^2}\int_0^{\pi/2}d\vartheta_\downarrow\sin 2\vartheta_\downarrow D_\downarrow \quad (21)$$

$$+\frac{e^2p_S^2A}{8\pi^2}\int_0^{\pi/2}d\vartheta_N\sin 2\vartheta_N D_\uparrow.$$

Equations (19)–(21) are valid for arbitrary transmission coefficients D_α. For particular calculations of $G_A(V=0)$, we will use the model equations for transmission coefficients corresponding to direct contact between the metals

$$D_\uparrow = \frac{4p_{x\uparrow}p_{xs}}{(p_{x\uparrow}+p_{xs})^2}, \quad D_\downarrow = \frac{4p_{x\downarrow}p_{xs}}{(p_{x\downarrow}+p_{xs})^2}. \quad (22)$$

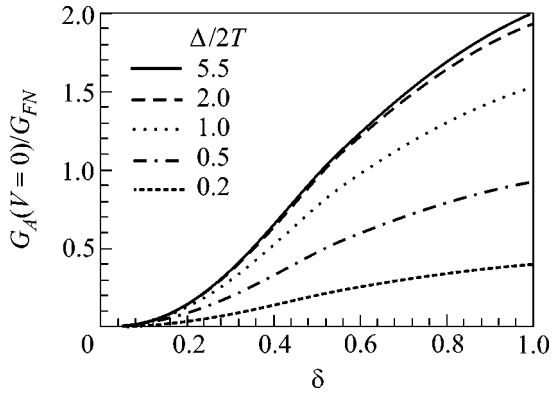

Fig. 1. Dependence of the normalized Andreev conductance on the ratio δ of the Fermi momenta of spin subbands of the ferromagnet conduction band ($\delta = p_{F\downarrow}/p_{F\uparrow}$).

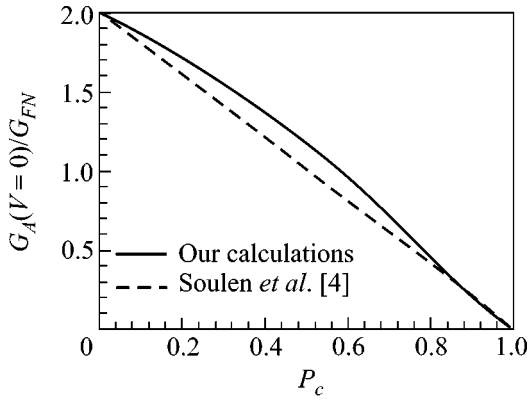

Fig. 2. Dependence of the normalized Andreev conductance on the contact polarization P_c.

With these transmission coefficients, $G_A(T = 0)$ and $G_{F/N}$ are calculated analytically:

$$G_{F/N} = \frac{e^2 p_S^2 A}{6\pi^2}\left(\frac{\delta_{N\uparrow}(1+\delta_{N\uparrow})}{(1+\delta_{N\uparrow})^2} + \frac{\delta_{N\downarrow}^3(2+\delta_{N\downarrow})}{(1+\delta_{N\downarrow})^2}\right). \quad (23)$$

For $G_A(T = 0)$, Eq. (12) is obtained. Here, $\delta_{N\uparrow} = p_S/p_{F\uparrow}$ and $\delta_{N\downarrow} = p_{F\downarrow}/p_S$. From Eqs. (12) and (23) it follows that the Andreev conductance at $\delta < 0.26$ becomes smaller than the conductance of the contact in the normal state. The dependence of the ratio $G_A(V = 0)/G_{F/N}$ measured in [4] on the parameter δ is given for various temperatures in Fig. 1. The ratio $\Delta/2T = 5.5$ corresponds to the experimental conditions [4] ($T = 1.6$ K, $\Delta_{Nb} = 1.5$ meV). In order to universally interpret the experimental data obtained in [4] for a series of ferromagnetic materials in contact with superconducting Nb, we fixed the Fermi momentum of the superconducting metal by the equation $p_S^2 = (p_{F\uparrow}^2 + p_{F\downarrow}^2)/2 = \text{const}$. Now, the values of δ (abscissa) can be estimated by the value of the reduced conductance at zero voltage across the contact (ordinate). We emphasize that, in this calculation, we assumed the absence of an oxide or similar barrier at the F/S interface ($Z_{BTK} = 0$). The results of estimating δ are given in the table.

Table

Material under study [4]	δ	P_c (%)	P_c (%) [4]
NiFe	0.64	42	37 ± 5.0
Co	0.55	52	42 ± 2.0
NiMnSb	0.48	63	58 ± 2.3
LSMO	0.31	83	78 ± 4.0
CrO_2	0.18	94	90 ± 3.6

Note that the values δ(Ni) = 0.64 and δ(Co) = 0.55 obtained from Andreev spectroscopy turned out to be close to the upper estimates for δ(Ni) = 0.64 and δ(Co) = 0.57, which we obtained in [14] from data on giant magnetoresistance in magnetic point contacts [15].

Let us now pass to comparison with the original estimates of polarization obtained in [4]. The authors of [4] argue that the normalized conductance measured in that work depends on polarization as $G_{F/S}/G_n = 2(1 - P_I)$ (Eqs. (4)–(6) in [4]), where $P_I = (I_\uparrow - I_\downarrow)/(I_\uparrow + I_\downarrow)$ and $G_n \simeq G_{F/N}$ is the conductance at high voltages across the contact ($eV \gg \Delta$). In the course of discussion, the authors identified the current polarization P_I with the contact polarization $P_c = (N_\uparrow v_{F\uparrow} - N_\downarrow v_\downarrow)/(N_\uparrow v_{F\uparrow} + N_\downarrow v_\downarrow) = (1 - \delta^2)/(1 + \delta^2)$, where N_α and v_α are the density of states and the Fermi velocity in the α-spin subband of the ferromagnet, respectively. This identification is not quite correct, because it implicitly implies the independence of the total current $I_\uparrow + I_\downarrow$ through the contact in the normal phase from the spin polarization of the ferromagnet. It is evident from Eq. (23) that $G_{F/N}$ essentially depends on δ. As a result, the reduced conductance $G_A(V = 0)/G_{F/N}$ is a nonlinear function of the contact polarization P_c (Fig. 2). It is seen in Fig. 2 that the identification of P_I with P_c leads to a systematic underestimation of the estimate for P_c (see the third and the fourth columns of the table). Note here that the numerical calculations of the conductance at zero voltage performed in [11] (see Fig. 4 of that work for $Z = 0$, $T/T_c = 0.2$) fit the linear dependence on the contact polarization proposed in [4] well (dashed line in our Fig. 2). From here it follows that the calculations made in [11] also give underestimated values of the contact polarization estimated from the conductance at zero voltage.

Thus, a consistent quasiclassical theory of Andreev reflection in F/S nanocontacts has been constructed in this work. It allows, in particular, correct estimates to be made for the polarization parameter δ of the ferro-

magnet conduction band, through which the polarization of the density of states P_{DOS}, the tunneling polarization P_T, and the contact polarization P_c are expressed. Our analysis of experiments on Andreev spectroscopy leads to values of P_c that are systematically higher than those estimated previously.

We are grateful to G.B. Teĭtel'baum for the discussion of the results.

This work was supported by the Russian Foundation for Basic Research (project no. 00-02-16328) and by the program Universities of Russia Basic Research (project no. UR.01.01.061).

REFERENCES

1. A. F. Andreev, Zh. Éksp. Teor. Fiz. **46**, 1823 (1964) [Sov. Phys. JETP **19**, 1228 (1964)].
2. G. E. Blonder, M. Tinkham, and T. M. Klapwijk, Phys. Rev. B **25**, 4515 (1982).
3. M. J. M. de Jong and C. W. J. Beenakker, Phys. Rev. Lett. **74**, 1657 (1995).
4. R. J. Soulen, J. M. Byers, M. S. Osofsky, *et al.*, Science **282**, 85 (1998); J. Appl. Phys. **85**, 4589 (1999).
5. S. K. Upadhyay, A. Palanisami, R. N. Louie, and R. A. Buhrman, Phys. Rev. Lett. **81**, 3247 (1998).
6. B. Nadgorny, R. J. Soulen, M. S. Osofsky, *et al.*, Phys. Rev. B **61**, 3788(R) (2000).
7. Y. Ji, G. J. Strijkers, F. Y. Yang, *et al.*, Phys. Rev. Lett. **86**, 5585 (2001).
8. G. J. Strijkers, Y. Ji, F. Y. Yang, and C. L. Chien, Phys. Rev. B **63**, 104510 (2001).
9. S. Kashiwaya, Y. Tanaka, N. Yoshida, and M. R. Beasley, Phys. Rev. B **60**, 3572 (1999).
10. A. A. Golubov, Physica C (Amsterdam) **326–327**, 46 (1999).
11. K. Kikuchi, H. Imamura, S. Takanashi, and S. Maekava, Phys. Rev. B **65**, 20508 (2001).
12. A. I. Larkin and Yu. N. Ovchinnikov, J. Low Temp. Phys. **10**, 401 (1973).
13. A. V. Zaĭtsev, Zh. Éksp. Teor. Fiz. **86**, 1742 (1984) [Sov. Phys. JETP **59**, 1015 (1984)].
14. L. R. Tagirov, B. P. Vodopyanov, and K. B. Efetov, Phys. Rev. B **65**, 214419 (2002).
15. N. Garcia, M. Munoz, and Y.-W. Zhao, Phys. Rev. Lett. **82**, 2923 (1999); Phys. Rev. Lett. **83**, 2030 (1999).

Translated by A. Bagatur'yants

JETP Letters, Vol. 77, No. 3, 2003, pp. 132–134. Translated from Pis'ma v Zhurnal Éksperimental'noĭ i Teoreticheskoĭ Fiziki, Vol. 77, No. 3, 2003, pp. 159–161.

Possible Superconductivity Mechanism in High-Temperature Superconductors

I. I. Amelin

Mordovian State University, ul. Bol'shevistskaya 68, Saransk, 430000 Russia

Received December 19, 2002

The formation temperature ($T^* \sim 135$ K) is determined in the Shubin–Vonsovski approximation for local electron pairs in the CuO_2 planes of $YBa_2Cu_3O_7$ crystal. This estimate is used to obtain the Coulomb pseudopotential $\mu^* \approx -0.15$. In the presence of strong electron–phonon coupling ($\lambda \sim 0.5$) and electron correlation in the electron pairing, the estimate of critical temperature $T_c \approx 99$ K agrees, by the order of magnitude, with its experimental value. The calculated ratio $2\Delta/kT_c \approx 4.13$ confirms the presence of strong electron pairing. © *2003 MAIK "Nauka/Interperiodica".*

PACS numbers: 74.20.-z; 74.72.Bk

The formation of charge-density waves (CDWs) in the anionic subsystem of the CuO_2 planes of high-temperature superconductors (HTSCs) in which the Shubnikov–Vonsovski conditions are met was predicted in [1]. Experiments confirmed the occurrence of this phenomenon [2]. The possible reasons for the formation of local electron pairs (LEPs) in the presence of the CDWs involving atomic vibrations were considered in [3]. The LEP-formation temperature T^* depends on the number of holes, $t_1 < 1$ and $t < 1$, in the *p* and *d* states of, respectively, the O and Cu ions in the CuO_2 planes; estimates give $T^* \leq 155$ K. As the number t_1 of holes slightly increases and *t* slightly decreases, the temperature T^* changes in a bell-shaped fashion, in accordance with the experimental $T_c(\delta)$ dependence for $YBa_2Cu_3O_{6+\delta}$ crystal. This superconductivity model was used in [4] to propose a method of preparing HTSC materials with $t_1 = 1$ and $t = 1$ and, correspondingly, with high T^* and T_c. These conditions are likely met in the CuO–Cu interface. In this approximation, a rough estimate of the temperature gives $T^* \sim 10^4$ K [5]. For the concentration $n \sim 1.6 \times 10^{20}$ cm^{-3} in the interfacial layer and the carrier effective mass $m^* \sim m_e$, the temperature of the onset of Bose–Einstein condensation can be as high as $T_c \sim 1000$ K. This estimate of the T_c temperature corresponds, by the order of magnitude, to its experimental value [6]. Therefore, to obtain room-temperature superconductivity (RTSC), the materials should have, in all likelihood, the layered structure of the type …–Cu–CuO–Cu–CuO–… .

Abundant experimental evidence, including measurements of isotope effect in the HTSC materials, indicates that the formation of the superconducting (SC) state is due to the electron–phonon interaction (EPI). The electron–electron interactions should also be involved in the formation of the SC state. The standard BCS formulas for T_c or their generalization to the case of strong electron–phonon coupling give [7]

$$T_c = \omega_{ph} \exp\left\{-\frac{1+\lambda}{\lambda-\mu^*}\right\}, \quad (1)$$

where $\mu^* = \mu/(1 + \mu\ln(B/\omega_{ph}))$ is the Coulomb pseudopotential, *B* is the band halfwidth, and ω_{ph} is the energy of atomic vibrations. For the electronic Coulomb interaction *U* and the density of states $N(0)$ per one spin at the Fermi level, one has $\mu = UN(0)$.

In my opinion, the formation of the SC state in the HTSC and M_3C_{60} systems has a common nature. The values $N(0) \approx 10$–14 eV/spin, derived from the paramagnetic susceptibility measurements, are reported in [8] for narrow-band M_3C_{60} systems with $B \approx 0.25$ eV. In the HTSC materials, CuO_2 planes also have a narrow *p* subband with $B \sim 0.4$ eV [3] and with the density of states as high as $N(0) \approx 10$ eV/spin. In this class of compounds, the heat-capacity jump $\Delta C/T_c$ has nearly the same value: 75 (Rb_3C_{60}), 68 (K_3C_{60}) [8], and 67 mJ/(K^2 mol) (YBCO-123) [9]. The corresponding heat-capacity jump per mole is equal to $\Delta C \approx 0.72R$ ($R = N_Ak$). A heat-capacity jump as large as this is sometimes interpreted as a confirmation of the Bose condensation of electron pairs existing above T_c; i.e., $\Delta C = Nk$, where *N* is the number of these pairs (on the order of the total number of particles) and *k* is the Boltzmann constant [9]. From my point of view, the large heat-capacity jump is indicative of the strong coupling and, hence, is accompanied by a sizable rearrangement of the electron system with density $n \approx 10^{21}$ cm^{-3} and the carrier effective mass $m \sim 1$–$2m_e$. Since these systems exhibit isotope shift, it is clear that the atomic vibrations must be taken into account in the formation

of the SC state. According to [10], the Debye temperature of materials composed of C atoms is $\Theta_D = 2230$ K (0.19 eV). The typical energies ω_{ph} of C vibrations in the C_{60} molecule are 0.034–0.195 eV [8]. Since the mass of the O atom is also small and is comparable, by the order of magnitude, with the mass of C atom, the mean vibrational energy of O anions in the HTSC materials is likely to be $\omega_{ph} \sim 10^3$ K (0.086 eV).

The estimate $\lambda \approx 0.4$–0.8 and the experimental value of the ratio $2\Delta/kT_c \approx 5$ in the YBCO crystal are given in [9]. From experimental studies [11], it follows that electron pairing due to the electron–phonon interaction is complemented by electron correlation, which also must be taken into account when explaining the SC state of an HTSC. The estimate $\lambda \approx 0.6$ was obtained for $YBa_2Cu_3O_7$ with allowance made for the electron correlation at $\Theta_D \approx 400$ K. In conventional broad-band superconductors, the parameters λ and Θ_D are $\lambda \sim 0.4$–1.0 and $\Theta_D \sim 400$ K [12]. For HTSC and M_3C_{60} materials with narrow conduction bands and high vibrational energy $\omega_{ph} \sim 10^3$ K of light O and C atoms (and, correspondingly, high EPI energies and $N(0) \sim 10$ eV/spin), the estimate $\lambda \approx 0.4$–0.5 is quite realistic. Let us take $\lambda \approx 0.5$ for the electron–phonon coupling in the YBCO crystal. In the absence of EPI, the LEP-formation energy in YBCO is $T^* \approx 135$ K (0.012 eV) [3]. Inasmuch as our interest is with the electron-pairing energy, the cited energy corresponds to the attraction energy, and then $U = -T^*$ and $\mu \approx -T^*N(0) \approx -0.12$. The calculation of the pseudopotential yields $\mu^* \approx -0.15$. Substituting these parameters in Eq. (1), one obtains the estimate $T_c \approx 99$ K, which is close to the experimental value. One can note in conclusion that the parameter T^* is equal to T_c by the order of magnitude; i.e., $T_c \sim T^*$. Since the $T^*(\delta)$ curve for the $YBa_2Cu_3O_{6+\delta}$ crystal is bell-shaped [3], Eq. (1) for $T_c(\delta)$ is in agreement with the experimental $T_c(\delta)$ dependence.

The isotope effect provides important information on the superconductivity mechanism. In the BCS theory, the transition temperature for systems with like ions of mass M behaves as $T_c \sim M^{-\alpha}$, where $\alpha = 0.5$. From this relation it follows that the temperature T_c for materials consisting of light atoms should be rather high. Assuming that the SC state in HTSC materials is due to EPI alone, one obtains, after substituting λ and $\mu^* = 0$ in Eq. (1), $T_c \approx 50$ K.

The authors of [13] have studied the A_xC_{60} system with $A = Br_3CH$, for which the critical temperature is $T_c = 117$ K. The experimental and theoretical studies of M_xC_{60} fullerides were reviewed in [8]. Estimates were obtained for the parameters that are necessary in the calculation of T_c. The values obtained for the parameters ω_{ph} and λ were, basically, the same as those typical of HTSC materials, except for the parameter B, whose value is $B = 0.25$ eV for M_3C_{60}. In the Shubin–Vonsovski approximation, preliminary estimates of the temperature T^* for the M_3C_{60} and A_xC_{60} systems give 21 and 105 K, respectively. These values correspond, respectively, to the Coulomb pseudopotential $\mu^* = -0.02$ and -0.1. Substituting the values of parameters μ^*, $\lambda = 0.5$, and B in Eq. (1), one obtains $T_c = 56$ and 82 K for M_3C_{60} and A_xC_{60}, respectively. It is likely that λ is somewhat lower for M_3C_{60}. For $\lambda = 0.4$ and $\mu^* = 0$, the temperature $T_c \approx 30$ K corresponds to its experimental value; i.e., the EPI governs the formation of the SC state in M_3C_{60}. It is pointed out in [8] that the parameter $N(0)$ in the M_3C_{60} systems depends on the distance d between two C atoms of the neighboring C_{60} molecules as $N(0) \sim d^a$ with $a = 2.7$. This is due to the fact that B decreases with increasing d, leading to an increase in $N(0)$ and λ. Crystal-lattice studies of A_xC_{60} suggest [13] that d is larger than d in M_3C_{60}. Let us take $N(0) \approx 15$ eV/spin and $\lambda \approx 0.6$; this gives $\mu^* = -0.15$ and, correspondingly, $T_c \approx 122$ K.

It is pointed out in [8] that the ratio $2\Delta/T_c$, where Δ is the superconducting gap in the HTSC and M_xC_{60} systems, exceeds the BCS value 3.53. This points to the strong electron-pairing effects in these materials. In the strong-coupling case, the formula given in [8] for this ratio is

$$\frac{2\Delta}{kT_c} = 3.53\left[1 + 12.5\left(\frac{T_c}{\omega_{ln}}\right)^2 \ln\left(\frac{\omega_{ln}}{2T_c}\right)\right], \qquad (2)$$

where ω_{ln} is the logarithmic mean phonon frequency. By substituting ω_{ln} and T_c, one obtains for YBCO $2\Delta/kT_c \approx 4.1$. The corresponding experimental value is $2\Delta/kT_c \approx 5$ [9].

At present, there is much discussion on the mechanism of superconductivity in the HTSC materials. For example, the SC state in some works is attributed to the antiferromagnetic fluctuations in current-carrying CuO_2 planes. In this case, the state of the Cu ion should be close to the Cu^{2+} state [9]. However, spectroscopic data suggest that holes are more likely located on the oxygen atoms, whose valence becomes close to –1 [14]. Superexchange between the magnetic moments of the Cu^{2+} ions via the filled oxygen p orbitals gives rise to the antiferromagnetic ground state. If, however, only one electron is placed at the oxygen p orbital, the superexchange will be favorable to the ferromagnetic ordering of the Cu^{2+} magnetic moments; i.e., a region with a tendency to ferromagnetic ordering arises near a hole localized on oxygen. From this it follows that the appearance of holes at the oxygen orbitals is accompanied by the strengthening of the competing magnetic interaction, which, starting with a certain critical hole concentration, strongly suppresses the Néel antiferromagnetic state. As a result, the Néel temperature diminishes, and the system of local magnetic moments of Cu^{2+} undergoes transition to a nonmagnetic state. In addition, the Cu ions tend to the Cu^{1+} state upon doping the CuO_2 planes of YBCO crystal [3, 15]. Experiments

on measuring the magnetic moments and the Néel temperature of YBCO confirm this point of view [16].

Analyzing the above, one can conclude that the model suggested for the formation of the SC state in HTSC materials explains the following experimental findings:

(1) The presence of Bose particles and a pseudogap at $T > T_c$; this was confirmed experimentally by the HTSC studies in [17]. In [18], the pseudogap formation was explained by the quasiparticle local pairing without phase coherence between the pairs;

(2) Large heat-capacity jump upon the transition to the SC state;

(3) The value of critical temperature T_c;

(4) The bell-shaped $T_c(\delta)$ curve for the $YBa_2Cu_3O_{6+\delta}$ crystal;

(5) The rise in T_c at high pressure as a result of strengthening the electron–electron interaction between centers;

(6) Sharp drop in T_c in the presence of oxygen vacancies and upon substituting Zn ions for the Cu ions in the CuO_2 planes, as a result of a change in the electron–electron interactions between centers;

(7) The value of $2\Delta/kT_c$; and

(8) The temperature $T_c = 10^3$ K in the Cu–CuO interface.

REFERENCES

1. I. I. Amelin, Sverkhprovodimost: Fiz., Khim., Tekh. **4**, 1073 (1991).
2. A. I. Golovashkin and A. P. Rusakov, Usp. Fiz. Nauk **170**, 192 (2000) [Phys.–Usp. **43**, 184 (2000)].
3. I. I. Amelin, Pis'ma Zh. Éksp. Teor. Fiz. **70**, 24 (1999) [JETP Lett. **70**, 23 (1999)].
4. I. I. Amelin, Zh. Fiz. Khim. **73**, 2274 (1999).
5. I. I. Amelin, Pis'ma Zh. Éksp. Teor. Fiz. **76**, 219 (2002) [JETP Lett. **76**, 185 (2002)].
6. V. V. Osipov, I. V. Kochev, and S. V. Naumov, Zh. Éksp. Teor. Fiz. **120**, 1246 (2001) [JETP **93**, 1082 (2001)].
7. *Problems in High-Temperature Superconductivity*, Ed. by V. L. Ginzburg and D. A. Kirzhnits (Nauka, Moscow, 1977), p. 110.
8. O. Gunnarsson, Rev. Mod. Phys. **69**, 575 (1997).
9. N. M. Plakida, *High-Temperature Superconductors* (Mezhdun. Progr. Obraz., Moscow, 1996), p. 195.
10. C. Kittel, *Introduction to Solid State Physics*, 5th ed. (Wiley, New York, 1976; Nauka, Moscow, 1978).
11. A. L. Solovjov, V. M. Dmitriev, H.-U. Habermeier, *et al.*, Phys. Rev. B **55**, 8551 (1997).
12. E. G. Maksimov, D. Yu. Savrasov, and S. Yu. Savrasov, Usp. Fiz. Nauk **167**, 353 (1997) [Phys.–Usp. **40**, 337 (1997)].
13. J. H. Schön, Ch. Kloc, and B. Batlogg, Science **293**, 2432 (2001).
14. G. S. Grader, P. K. Gallagher, and A. T. Fiory, Phys. Rev. B **38**, 844 (1988).
15. I. I. Amelin, Fiz. Nizk. Temp. **22**, 539 (1996) [Low Temp. Phys. **22**, 415 (1996)].
16. J. Rossat-Mignod, L. P. Regnault, S. Vettier, *et al.*, Physica C (Amsterdam) **185–189**, 86 (1991); Physica B (Amsterdam) **180–181**, 383 (1992); L. P. Regnault, P. Bourges, P. Barlet, *et al.*, Physica C (Amsterdam) **235–240**, 59 (1994).
17. V. F. Gantmakher, R. A. Emel'chenko, I. G. Naumenko, and G. É. Tsydynzhapov, Pis'ma Zh. Éksp. Teor. Fiz. **72**, 33 (2000) [JETP Lett. **72**, 21 (2000)].
18. R. Emery and P. Kivelson, Nature **374**, 434 (1995).

Translated by V. Sakun

JETP Letters, Vol. 77, No. 3, 2003, pp. 135–139. From Pis'ma v Zhurnal Éksperimental'noĭ i Teoreticheskoĭ Fiziki, Vol. 77, No. 3, 2003, pp. 162–166.

Unconventional Magnetoresistance in Long InSb Nanowires¶

S. V. Zaitsev-Zotov[1], Yu. A. Kumzerov[2], Yu. A. Firsov[2], and P. Monceau[3]

[1] *Institute of Radioengineering and Electronics, Russian Academy of Sciences, Moscow, 101999 Russia*
e-mail: serzz@cplire.ru

[2] *Ioffe Physicotechnical Institute, Russian Academy of Sciences, St. Petersburg, 194021 Russia*

[3] *Centre de Recherches sur Les Très Basses Températures, 38042 Grenoble, Cédex 9, France*

Received December 25, 2002

Magnetoresistance in long correlated nanowires of degenerate semiconductor InSb in asbestos matrix (wire diameter of around 5 nm, length 0.1–1 mm) is studied in the temperature range 2.3–300 K. At zero magnetic field, the electric conduction G and the current–voltage characteristics of such wires obey the power laws $G \propto T^{\alpha}$, $I \propto V^{\beta}$, expected for one-dimensional electron systems. The effect of the magnetic field corresponds to a 20% growth of the exponents α, β at $H = 10$ T. The observed magnetoresistance is caused by the magnetic-field-induced breaking of the spin–charge separation and represents a novel mechanism of magnetoresistance.

PACS numbers: 73.63.Nm; 72.15.Gd

Electron–electron correlation effects being negligible in the three-dimensional case, they play a dominant role in one dimension. One of the most significant consequences of the correlation effect is the absence of quasiparticle excitations in 1D metals. Instead, in the 1D case, collective excitations associated with separate spin and charge degrees of freedom are developed and lead to the formation of the so-called Luttinger liquid (LL) (for a review, see [1]). The spin–charge separation mentioned above means different velocities for collective charge and spin excitations. Charge transport in LL is of a collective nature and cannot be described by the conventional kinetic equations. A charged impurity in a 1D electron system forms a tunneling barrier. The absence of single-particle excitations complicates the tunneling of electrons in LL and leads to a power law dependence of a tunneling density of states. Tunneling through this barrier in the case of short-range e–e interaction provides the power laws for the linear conduction [2] $G(T) \propto T^{\alpha}$ and nonlinear I–V curve $I(V) \propto V^{\beta}$, whereas, for the long-range Coulomb interaction, a substantially different functional dependence of type $G \propto \exp[-\nu \ln(T_0/T)^{1/3}]$ is predicted [3, 4].

Experimental study of 1D behavior remains a challenge. Single-wall and multiwall carbon nanotubes and various nanowires have been intensively studied in recent years (see, e.g., [5–7] and references therein). One of the most dramatic effects of reduced dimensionality on the physical properties of long nanowires was reported recently for the electric conduction of InSb nanowires in an asbestos matrix [8]. It was found that G as a function of temperature and electric field follows power laws over five orders of magnitude of conduction variation. The effect was considered a manifestation of the Luttinger-liquid-like behavior of an impure 1D electron system. This conclusion was supported recently by measurements of thermoelectric power [9]. Namely, it was found that the Seebec coefficient of InSb nanowires as a function of temperature exhibits a metallic behavior corresponding to n-type conduction, whereas the temperature variation of the electric conduction follows a power law. LL is the only known physical system where these both types of behavior coexist [10].

The physical reason for the realization of the LL-like behavior in InSb nanowires is a lucky coincidence of numerous factors [8]. Namely, the very small effective electron mass intrinsic to bulk InSb ($m^* \sim 10^{-2} m_e$) is favorable for a pronounced energy-level splitting due to the quantum size effect, which was estimated to 10^4 K in our nanowires being 5 nm in diameter [8]. Studied samples consist of about 10^6 of such parallel crystalline [11] InSb nanowires forming a hexagonal lattice with a 30-nm period. Thus, long-range interactions between electrons in each wire may be screened through the Coulomb interaction of these electrons with electrons on neighboring wires. This leads to short-range intrawire e–e interactions, which is a basic assumption of the LL theory. In all other respects, the wires can be considered independent of each other. It was argued [8] that the transport properties of individual wires are determined by tunneling through impurities and weak links (e.g., constrictions) introduced during the fabrication process. Thus, such an impure LL may be considered [8] as broken into drops of almost pure LL separated by weak links. "Almost pure" means that the size of most of the drops is less than the local-

¶ This article was submitted by the authors in English.

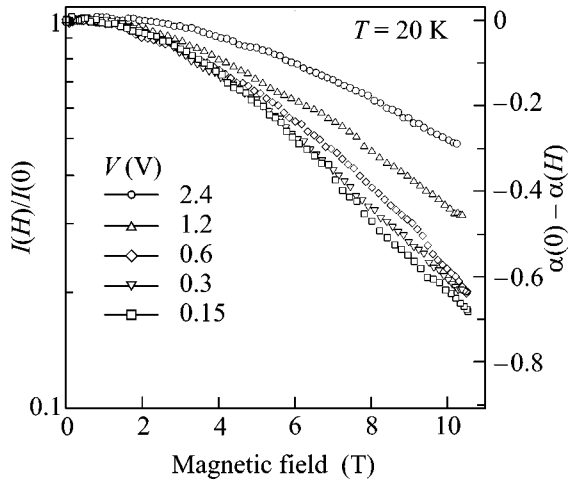

Fig. 1. Typical set of $I(H)$ curves measured at different voltages. The right axis scale corresponds to the estimate $\alpha(0) - \alpha(H) = \ln[I(T, H)/I(T, 0)]/\ln(\epsilon/T)$ at $T = 20$ K. $H \perp I$. Sample 2, $\epsilon = 250$ K.

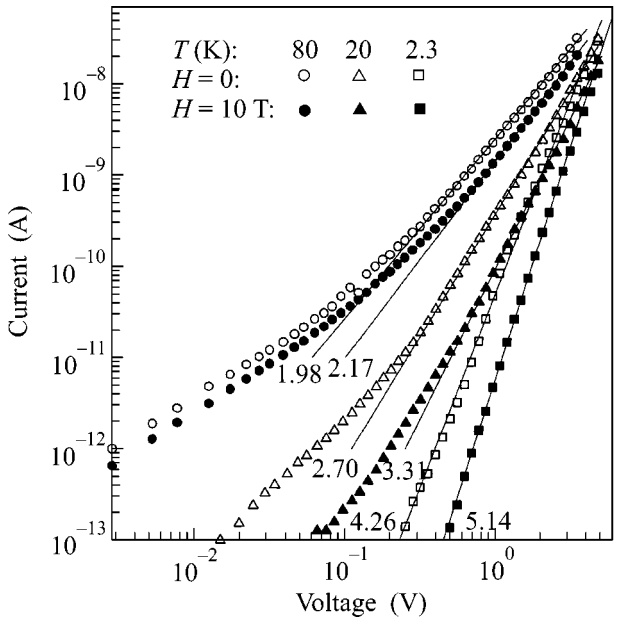

Fig. 2. Temperature set of I–V curves measured at zero magnetic field (empty patterns) and at $H = 10$ T (filled patterns). $H \perp I$. Sample 2. Solid lines show the best fit of the nonlinear part by the power law, $I \propto V^{\beta}$. The respective exponents, β, are indicated by numbers.

ization length L_{loc}. If one takes into account the repulsive e–e interaction, L_{loc} may be larger than the mean distance between impurities and the mean free path (weak pinning) [12, 13]. As the mean drop size is $\sim 10^3$ nm [8], this condition can be fulfilled. Then the dominant role in transport is determined by tunneling through weak links, which are connected in series by LL drops, as was proposed in [14]. In addition, due to the high density of weak links along each nanowire, contact effects play a negligible role in transport properties.

Study of the magnetoresistance is a powerful tool for investigation of the transport mechanism in physical systems. In the case of LL, where charge and spin degrees of freedom are decoupled, the magnetic field effect can yield new features that are not observed in other physical systems. In particular, it causes breaking of the spin–charge separation [15]. As a result, the charge mode responsible for electric conduction gets a contribution from the spin mode. This effect is expected to be most pronounced in TDOS and affects the critical indices [16]. So, a novel type of magnetoresistance can be expected in physical systems exhibiting LL-like behavior, whose conduction is dominated by tunneling. In this context, InSb nanowires are very promising objects because of their exceptionally strong spin–orbit coupling, which leads to a very high g factor of $g \approx 50$. Below, we present magnetoresistance data for InSb nanowires in an asbestos matrix in magnetic fields up to 10 T. The observed magnetoresistance corresponds to a magnetic-field dependence of the exponents α, β caused by magnetic-field-induced breaking of the spin–charge separation, representing a novel mechanism of magnetoresistance.

We have studied the electrical conduction of long InSb nanowires crystallized inside an asbestos matrix as a function of magnetic field, temperature, and electric field. Sample preparation and characterization have been described in detail elsewhere [8, 11]. The data reported below were obtained for two representative samples demonstrating LL-like behavior with zero magnetic field exponents $\alpha = 2.2$, $\beta = 2.1$ (sample 1), $\alpha = 4.5$, $\beta = 4.3$ (sample 2). The magnetoresistance of both samples demonstrates a similar behavior.

Figure 1 shows a typical variation of the electric current I measured at a set of fixed voltages versus magnetic field. Magnetoresistance in low magnetic fields is negative, as observed in a network of single-wall carbon nanotubes [17]. Conduction reaches a maximum at $H \approx 1$ T and falls by a factor of 5 at $H = 10$ T at a given temperature. For relatively small voltages (corresponding to the linear conduction regime), the effect of magnetic field on the conduction is practically independent of the voltage. For larger voltages, the magnetoresistance is smaller. The observed magnetoconduction is slightly anisotropic, and the ratio $[I(H) - I(0)]/I(0)$ for $H \perp I$ is approximately 20% larger than for $H \parallel I$.

Figure 2 shows the effect of the magnetic field on the shape of I–V curves. At relatively high temperatures (80-K curve), the effect of magnetic field is small. At lower temperatures, the effect is much more pronounced (up to one order of magnitude at $T \leq 5$ K for $H > 10$ T) and is smaller for larger electric fields. For comparison, measurements on InSb extracted from

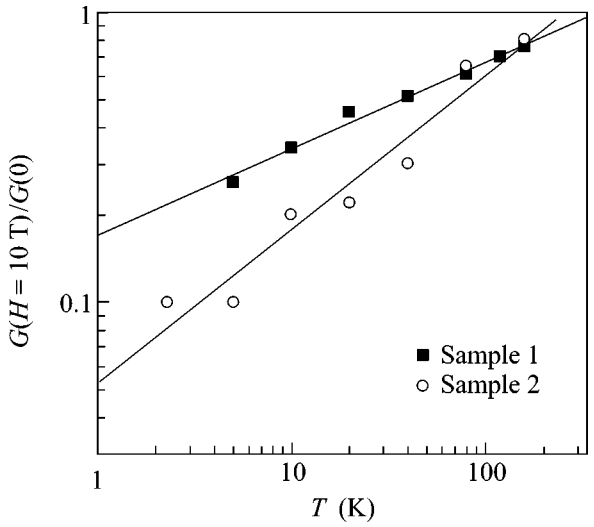

Fig. 3. Temperature dependence of the conduction in a magnetic field of 10 T related to its value at $H = 0$ measured at the smallest V. Lines indicate the least-squares fit of the data using the power law (Eq. (1)). $H \perp I$.

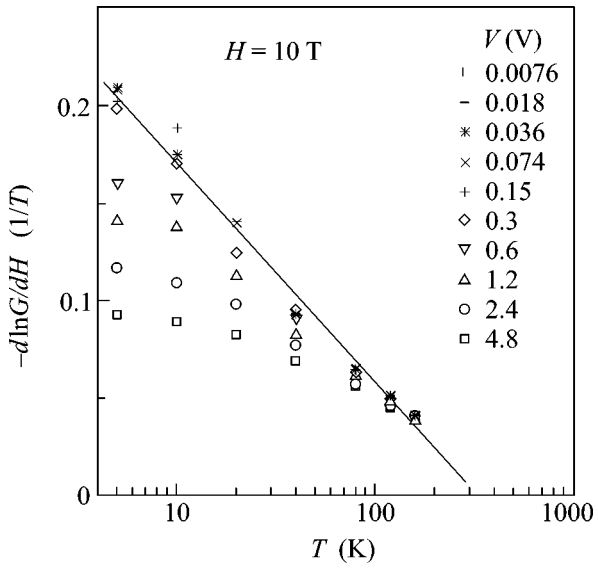

Fig. 4. Temperature dependences of the conduction sensitivity to the magnetic field $d\ln G/dH$ at $H = 10$ T for given values of the voltage V. The line corresponds to the power law $d\ln G/dH = 0.048\ln(T/315\ \mathrm{K})$ 1/T. $H \perp I$. Sample 1.

asbestos cracks showed only a 20% negative magnetoconduction $G(0) - G(H) \propto H^2$ at $T = 4.2$ K and $H = 10$ T, and magnetoresistance of InSb in vycor glass with a 7-nm channel network [18] is negligibly small. The magnetoresistance of a network of carbon nanotubes is also small [19]. These results demonstrate the decisive role of the one-dimensional sample topology. In addition, as seen from the low-temperature curves in Fig. 2, the magnetic field changes the slope of the nonlinear part of the curve, i.e., affects the exponent β.

Figure 3 shows the temperature variation of the ratio $G(H = 10\ \mathrm{T})/G(0)$. For sample 2 at $T < 20$ K, this ratio was estimated from the low-current part of I–V curves. It is clearly seen that the magnetoconduction depends on temperature and grows with decreasing temperature approximately as a power function of temperature.

$d\ln G/dH$ at $H = 10$ T as a function of both temperature and electric field is shown in Fig. 4. At relatively small voltages, $d\ln G/dH$ is practically independent of voltage and forms a limiting dependence. This dependence as a function of $\ln T$ can be approximated by a straight line, $d\ln G/dH = A - B\ln(T)$ (solid line in Fig. 4). At relatively large voltages, $d\ln G/dH$ tends to deviate from the limiting dependence upon cooling, the deviation growing with the voltage.

Temperature sets of $d\ln G/dH$ plotted versus voltage show a similar behavior (see Fig. 5). The high-voltage data form a limiting curve, which can be approximated by $d\ln G/dH = C - D\ln(V)$ (solid line in Fig. 5). Low-voltage data demonstrate a deviation from this limiting curve and are practically independent of voltage at $V \longrightarrow 0$. Note that the limiting curves in Figs. 4 and 5 are formed with different data; namely, the low-voltage data forming the limiting curve in Fig. 4 sit on the low-voltage plateaus in Fig. 5, and vice versa, the low-temperature data forming the limiting curve in Fig. 5 sit on the low-voltage plateaus in Fig. 4. Thus, Figs. 4 and 5 illustrate different features of the observed magnetoresistance.

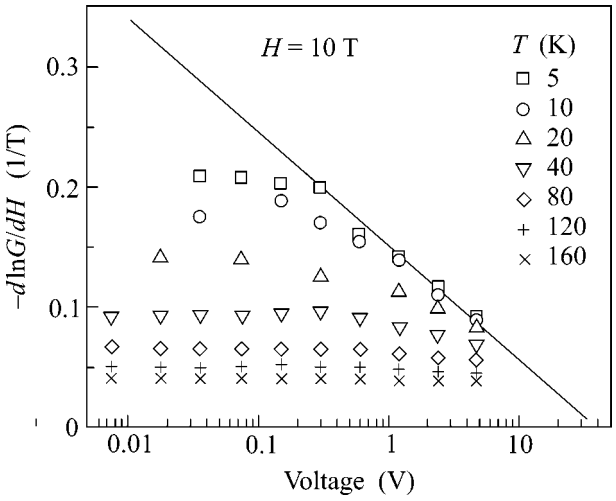

Fig. 5. Voltage dependences of the conduction sensitivity to the magnetic field $d\ln G/dH$ at $H = 10$ T for given temperatures. The line corresponds to the power law $d\ln G/dH = 0.041\ln(V/40\ \mathrm{V})$ 1/T. $H \perp I$. Sample 1.

As is clear from the data of Figs. 2–5, the observed magnetoresistance corresponds to a magnetic-field-induced variation of the exponents for $G(T)$:

$$G(T) = G_0\left(\frac{T}{\epsilon}\right)^{\alpha(H)} \quad (1)$$

and nonlinear I–V curve

$$I(V) = I_0\left(\frac{V}{V_0}\right)^{\beta(H)}. \quad (2)$$

Indeed, in this case $G(H)/G(0) = T^{\alpha(H)-\alpha(0)}$, in agreement with Fig. 3, $d\ln G/dH = (\ln T - \ln\epsilon)d\alpha/dH$ and $d\ln I/dH = (\ln V - \ln V_0)d\beta/dH$, in agreement with Figs. 4 and 5, respectively. Equations (1) and (2) fit the data with $d\alpha/dH = 0.05$ 1/T, $d\beta/dH = 0.06$ 1/T, and $\epsilon = 335$ K for sample 1, and 0.11 1/T, 0.12 1/T, and 250 K for sample 2 at $H = 10$ T. $\alpha(0) - \alpha(H)$ for sample 2 calculated with Eq. (1) and $\epsilon = 250$ K is shown in Fig. 1 (right scale).

Magnetic field affects both the orbital motion and the spin degree of freedom of electrons. While the magnetic length $L_B = \sqrt{c\hbar/eB} > d$, where d is the wire diameter, we cannot expect that orbital effects [20] play a role. In our 5-nm-diameter nanowires, this condition is broken at $B \sim 40$ T, far away from the maximum magnetic field 10 T used in our measurements. Thus, we can conclude that Zeeman splitting is responsible for the observed behavior. This splitting in InSb is especially strong due to the large g factor in InSb ($g \approx 50$).

At present, there is no theory describing magnetoresistance in 1D correlated conductors. We expect that magnetic field leads to a variation of α and β. It is known that magnetic field affects the correlation function critical exponents in the 1D Hubbard model [21], so $\alpha(H)$ and $\beta(H)$ dependences are expected. It is also worth mentioning that magnetic-field-dependent exponents are observed in the temperature variation of NMR relaxation time of a spin-1/2 Heisenberg ladder gapless phase [22]. Spin–charge separation in the LL model means that only independent collective spin (spinons) and charge (holons) excitations are present at $H = 0$. A magnetic field acting on the spin subsystem mixes spinons and holons and destroys thereby the spin-charge separation [15]. The magnetic-field dependence of a holon's characteristics (e.g., velocity) caused by breaking of the spin–charge separation results in a variation of the exponents. In [16], linear magnetic-field dependences for exponents of spectral functions and bulk density of states, $\rho_{\text{bulk}}(\omega, H)$, are obtained for a pure LL. Namely, the magnetic field affects the index for the tunneling density of states as

$$\alpha_{\text{bulk}}(H) = \alpha_{\text{bulk}}(0)\left(1 + a\frac{H}{H_c}\right), \quad (3)$$

where $H_c = \epsilon_F/g\mu_B$, and $\alpha \approx 1$ in the strong coupling regime [16]. So, despite the absence of theoretical results for $\alpha_{\text{end}}(H)$ responsible for tunneling through a single impurity barrier in magnetic field, similar relative variation of α, β is expected. Then the observed 20% variation of exponents in a magnetic field of 10 T corresponds to $H_c \sim 50$ T, which is achieved at $\epsilon_F = 0.1$ eV [8].

To our knowledge, a magnetoresistance of the observed type and such a large value has not yet been reported for other physical objects exhibiting LL-like behavior. Namely, magnetoresistance of carbon nanotubes may be interpreted within the framework of the weak-localization scenario and Aharonov–Bohm effect [17] and also as due to the change in a magnetic field of the density of states at the Fermi energy [23] for noninteracting electrons. Reported magnetoresistance in Bi [6] and Sb [7] nanowires of comparable diameter (~10 nm) is much smaller (15% in Bi and 0.2% in Sb at 5 T) and even has the opposite sign (Sb). Strong anisotropic magnetoresistance of bulk samples of *n*-InSb with electron densities $n \sim 10^{16}$ cm^{-3} is observed in the quantum limit of applied magnetic field at $T = 1.5$ K [24]. In contrast with our data, it can be explained within a conventional transport theory without taking into account the decisive role of e–e interactions.

We would like to note that the consideration described above is valid while $L_B > d$, i.e., at $H < 40$ T. When $L_B < d$, orbital effects [20] take place. In addition, when $H > H_c \sim 50$ T, a spin effect is no longer expected. So, the physical mechanism of magnetoresistance is expected to be changed at $H = 40$–50 T.

Thus, InSb nanowires exhibit a strong positive magnetoresistance (up to one order of magnitude at $H = 10$ T) corresponding to a magnetic-field-induced variation of the exponents α and β in $G \propto T^{\alpha}$ and $I \propto V^{\beta}$. This variation is a manifestation of a novel physical mechanism of magnetoresistance specific for 1D systems.

S.V. Zaitsev-Zotov is grateful to CRTBT–CNRS for hospitality during the experimental part of research. This work was supported by CNRS through jumelage 19 between CRTBT and the Institute of Radioengineering and Electronics of the Russian Academy of Sciences, the Russian Foundation for Basic Research (project nos. 01-02-17739, 01-02-17771, and 02-02-17656), INTAS (project no. 02-474), and MNTP "Physics of Solid-State Nanostructures."

REFERENCES

1. J. Voit, Rep. Prog. Phys. **58**, 977 (1995).
2. C. L. Kane and M. P. A. Fisher, Phys. Rev. Lett. **68**, 1220 (1992); Phys. Rev. B **46**, 15233 (1992).
3. L. I. Glazman, I. M. Ruzin, and B. I. Shklovskii, Phys. Rev. B **45**, 8454 (1992).
4. M. Fabrizio, A. O. Gogolin, and S. Scheidl, Phys. Rev. Lett. **72**, 2235 (1994).
5. M. Bockrath, D. H. Cobden, J. Lu, *et al.*, Nature **397**, 598 (1999); C. Schonenberger and L. Forro, Phys. World **13**, 37 (2000).

6. J. Heremans, C. M. Thrush, Yu-Ming Lin, *et al.*, Phys. Rev. B **61**, 2921 (2000).
7. J. Heremans, C. M. Thrush, Yu-Ming Lin, *et al.*, Phys. Rev. B **63**, 085406 (2001).
8. S. V. Zaitsev-Zotov, Yu. A. Kumzerov, Yu. A. Firsov, and P. Monceau, J. Phys.: Condens. Matter **12**, L303 (2000).
9. M. V. Vedernikov, O. N. Urypin, B. M. Goltsman, *et al.*, in *Proceedings of MRS Fall Meeting, Symposium G, Boston* (2001).
10. C. L. Kane and M. P. A. Fisher, Phys. Rev. Lett. **76**, 3192 (1996).
11. S. B. Vakhushev, private communication.
12. A. Furusaki and N. Nagaosa, Phys. Rev. B **47**, 4631 (1993).
13. H. Maurey and T. Giamarchi, Phys. Rev. B **51**, 10833 (1995).
14. S. R. Renn and D. P. Arovas, Phys. Rev. B **51**, 16832 (1995).
15. T. Kimura, K. Kuroki, and H. Aoki, Phys. Rev. B **53**, 9572 (1996).
16. S. Rabello and Q. Si, Phys. Rev. Lett. (in press); cond-mat/0008065.
17. A. Bachtold, C. Strunk, C. Schonenberger, *et al.*, Nature **397**, 673 (1999).
18. V. A. Berezovets, private communication.
19. G. T. Kim, E. S. Choi, D. C. Kim, *et al.*, Phys. Rev. B **58**, 16064 (1998).
20. C. Biagini, D. L. Maslov, M. Yu. Reizer, and L. I. Glazman, Europhys. Lett. **55**, 383 (2001); Shan-Wen Tsai, D. L. Maslov, and L. I. Glazman, Phys. Rev. B **65**, 241102 (2002).
21. H. Frahm and V. E. Korepin, Phys. Rev. B **43**, 5653 (1991); M. Ogata, T. Sugiyama, and H. Shiba, Phys. Rev. B **43**, 8401 (1991).
22. G. Chaboussant, Phys. Rev. Lett. **80**, 2713 (1998).
23. S. Roche and R. Saito, Phys. Rev. Lett. **87**, 246803 (2001).
24. S. S. Murzin, A. G. M. Jansen, and E. G. Haanappel, Phys. Rev. B **62**, 16645 (2000).

JETP Letters, Vol. 77, No. 3, 2003, pp. 140–142. Translated from Pis'ma v Zhurnal Éksperimental'noĭ i Teoreticheskoĭ Fiziki, Vol. 77, No. 3, 2003, pp. 167–170.

Conversion of Acoustic Bending Vibration Frequency in a Freely Suspended Ferroelectric Liquid-Crystal Film

S. V. Yablonskii[1, 2], K. Nakano[1], M. Ozaki[1], and K. Yoshino[1]

[1] *Department of Electronic Engineering, Graduate School of Engineering, Osaka University, Osaka 565-0871, Japan*

[2] *Shubnikov Institute of Crystallography, Russian Academy of Sciences, Leninskiĭ pr. 59, Moscow, 117333 Russia*

Received December 26, 2002

A nonlinear acoustic effect was observed experimentally in a freely suspended ferroelectric liquid-crystal film. The effect consisted of a change in the frequency of the film bending vibrations under the action of a varying electric field. The up- and down-conversion efficiencies were found to be 50 and 30%, respectively. © *2003 MAIK "Nauka/Interperiodica".*

PACS numbers: 68.60.Bs; 68.15.+e; 73.50.Rb

Parametric up-conversion is widely used in optics as a method in which infrared radiation mixes with coherent heterodyne radiation in an optically nonlinear material [1]. The nature of vibrational systems with parametric interaction has no physical limitations. These may be electromagnetic, acoustic, and mechanical systems or their combinations. In this work, parametric frequency conversion is demonstrated by the example of mechanical vibrations of a freely suspended film obtained from a ferroelectric liquid crystal. In the experiment, electromechanically induced vibrations were used as a "pump" source [2], and acoustic vibrations caused by the periodic thermal expansion of the surrounding air were used as a transformed signal [3].

Contrary to a liquid crystal placed in a flat glass capillary, the surface of a freely suspended film can easily be deformed under the action of weak acoustic or electric fields [4]. From the mechanical point of view, such a film is a highly sensitive system whose vibrational motion can be described by the Rayleigh theory, which is based on the assumption that, in the absence of meniscus and surrounding gas, the system eigenfrequencies depend only on the isotropic surface tension σ and homogeneous two-dimensional density $\rho_s = h\rho_{LC}$, where ρ_{LC} is the film volume density and h is the film thickness, the latter being varied in practice from hundreds of molecular lengths to one bimolecular layer [5] (for an arbitrarily shaped plane membrane, the eigenfrequencies are $\nu \sim \sqrt{\sigma/\rho_s}$). In an actual situation, the mechanical vibrations of a film can be adequately described only if one takes into account energy dissipation (and its nonlinearity) caused by the viscous flow of the liquid crystal in the film plane and by the presence of surrounding atmosphere. In the presence of energy dissipation, the equation of motion of a freely suspended film bounded by a frame, ordinarily shaped like a rectangular or circular diaphragm, has the form of differential equation [2] with the additional nonlinear term Dz^2, where D is the so-called nonlinearity coefficient [1]:

$$2\sigma\Delta z + (f_{sz}(x, y)e^{i\nu_1 t} + \text{c.c.}) + (g_{sz}(x, y)e^{i\nu_2 t} + \text{c.c.}) = \frac{\eta_s}{a^2}\frac{dz}{dt} + \rho_s^{\text{eff}}\frac{d^2z}{dt^2} + Dz^2, \quad (1)$$

where c.c. stands for "complex conjugate"; z is the displacement of the film surface from its equilibrium position; a is the hole diameter; η_s is the surface viscosity of liquid-crystal film; $h = Nl$ is the film thickness; N is the number of smectic layers; l is the smectic-layer thickness; ν is frequency; $f_{sz}(x, y)$ and $g_{sz}(x, y)$ are the amplitudes of force surface densities periodically varying, respectively, with frequencies ν_1 and ν_2; and ρ_s^{eff} is the surface density equal to $\rho_{LC}h + \rho_{\text{air}}H$, where ρ_{air} is the air volume density and H is the height of the air column involved in the vibrational motion [6].

Equation (1) can be interpreted as the equation of linear acoustics in the presence of extraneous interactions characterized by the quadratic correction Dz^2. The nonlinear term Dz^2 in Eq. (1) accounts for the asymmetry of the reactive restoring force that acts on the surface of freely suspended film. It is this asymmetry that is the cause for the appearance of the sum and difference frequencies in the film bending-vibration spectrum.

Freely suspended films were obtained by the standard procedure described in [7]. A film of CS-1029 ferroelectric liquid crystal (crystal–SmC* (18–73°C)–SmA (73–85°C)–N* (85–95°C)–isotropic liquid) was obtained on a round hole, 5 mm in diameter, made in a 1-mm-thick glass platelet. The film was prepared at the temperature of the smectic *A* phase, followed by cooling to the smectic *C* phase. To remove static defects, the

film, as a rule, was held for several hours in the smectic *A* phase before measurement. To apply ac electric voltage, SnO_2 electrodes were put on the glass surfaces. The frame with the film was clamped on a thermostatted table. The film temperature was measured using a calibrated copper–constantan thermocouple. Film thickness was calculated from the reflection spectrum [7], and the reflection spectrum was recorded using a multichannel analyzer. Sinusoidal voltage with an amplitude varying from 1 to 120 V and frequency ν_1 induced film deformations periodic in time and space. The deformations appeared due to the electromechanical effect that resulted from the interaction of electric field with spontaneous polarization of the ferroelectric liquid crystal [2, 8]. The vibration amplitude was determined from the deviation of the reflected laser beam from an arbitrary film area. Measurements were made using a position-sensitive detector consisting of a slit diaphragm and a silicon photodiode (Fig. 1). A He–Ne-laser beam polarized along the direction of the driving low-frequency electric field *E* (*s* polarization) was directed at an angle of 45° to the film normal. The probed local area of the film was no larger than 0.5×0.5 mm^2. The photodiode current was analyzed by a Fourier spectrometer with a synchronous detector for measuring the first and second harmonics of the sinusoidal electric field. The measured first-harmonic signal was proportional to the amplitude of the film vertical displacement. The second-harmonic optical response was mainly an artifact that was caused by the nonlinearity of the position-sensitive detector, by a change in the *E*-even Fresnel reflection coefficient, and, finally, by the nonlinearity due to the asymmetry of the restoring force.

Simultaneously with the ν_1 vibrations, the ν_2 vibrations were externally induced in the film. To excite the ν_2 vibrations, modulated radiation *5* from a semiconductor laser periodically heated blackened film *6*, which, in turn, heated a closed air volume contacting freely suspended film *3* (Fig. 1). The periodic air temperature expansion resulted in a periodic film deformation, which was also detected by the position-sensitive detector from the deflection of laser beam. Figure 2 shows the frequency-dependent amplitude of the vibrations induced in a freely suspended film by the periodic heating of air and the ensuing periodic change in its volume. One can see that, despite the high volume viscosity of the smectic liquid crystal ($\eta[25°C] = 270$ mPa s), the spectrum displays a pronounced resonance character, and the vibration amplitude at a frequency of 1190 Hz exceeds the film vibration amplitude at low frequencies in the range $0 < \nu < 100$ Hz.

The main result illustrating parametric frequency conversion in the ferroelectric film is shown in Fig. 3. This figure demonstrates the Fourier spectrum of a mechanical response to two harmonic forces acting on the freely suspended film. The pump vibration was excited electromechanically at frequency ν_1 =

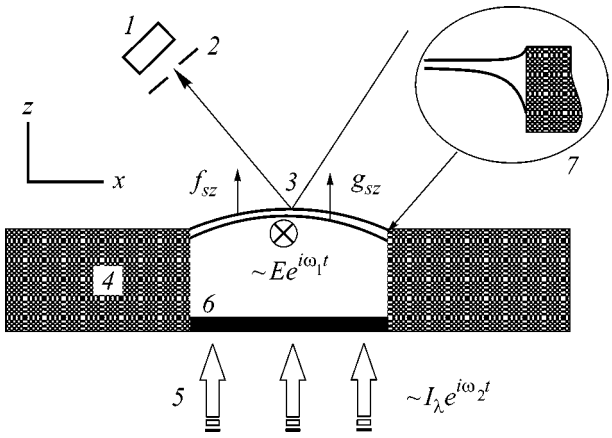

Fig. 1. Scheme of the experiment: *1* silicon photodiode; *2* slit diaphragm; *3* freely suspended film of ferroelectric liquid crystal CS-1029; *4* glass frame with a round hole 5 mm in diameter; *5* amplitude-modulated radiation of a semiconductor laser (λ = 650 nm, *W* = 25 mW); *6* thin (5-μm-thick) absorbing black-ink layer; and *7* magnified view of meniscus. The varying electric field *E* is directed perpendicular to the figure plane.

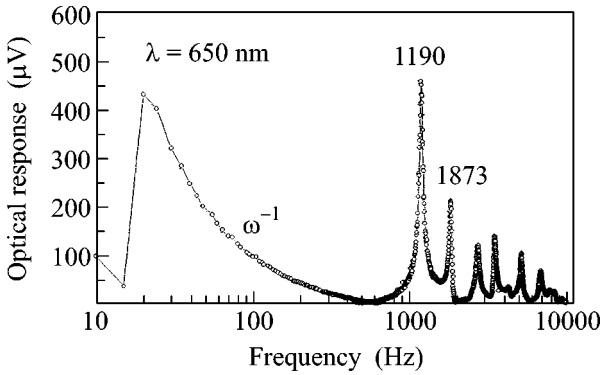

Fig. 2. Spectrum of mechanical vibrations induced in a freely suspended film by varying air pressure. A photodiode voltage of 10 mV corresponds to the 0.8-μm film displacement. The numbers near peaks indicate two first resonances in Hz (CS-1029; *N* = 345 layers; *l* = 2.8 nm, *T* = 23°C).

1259.692 Hz (slightly higher than the frequency of the first resonance maximum) and interacted with a relatively weak vibration that was excited at frequency ν_2 = 1873.389 Hz (second resonance maximum) by the variable air pressure. As a result of nonlinear interaction, two new vibrations at the sum ($\nu_1 + \nu_2$ = 3133.081 Hz) and difference ($\nu_1 - \nu_2$ = 613.697 Hz) frequencies appeared in the Fourier spectrum. In compliance with theory, the difference signal was noticeably weaker than the signal at the sum frequency [9] (the up- and down-conversion efficiencies were 50 and 30%, respectively).

It is worth noting that, by now, there has been amassed much evidence that freely suspended liquid-crystal films are organized in a more complicated fash-

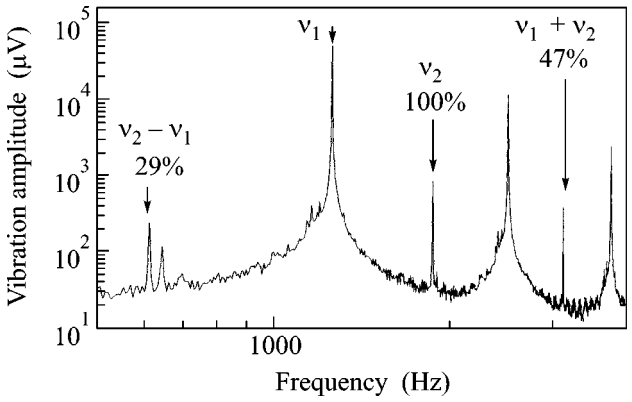

Fig. 3. The Fourier spectrum of the response of a freely suspended film (CS-1029; $N = 345$ layers) to the action of two harmonic forces. A varying sinusoidal voltage with the amplitude $U = 40$ V and frequency $\nu_1 = 1259.692$ Hz (accuracy of frequency determination was 0.001 Hz) was applied to the film. Simultaneously, the blackened film and hence air volume contacting the freely suspended film were heated by the amplitude-modulated radiation of a semiconductor laser at frequency $\nu_2 = 1873.389$ Hz ($\lambda = 650$ nm, W = 25 mW). The numbers in percent correspond to the degree of conversion of the mechanical vibration at frequency $\nu_2 = 1873.389$ Hz into the vibrations with the sum and difference frequencies (100%) corresponds to a signal voltage of 8.354×10^{-4} V).

ion than is predicted by the Rayleigh theory. It is reported in the literature that, in some cases, the mechanical properties of freely suspended films can be adequately described only if the additional factors are taken into account, such as volume elasticity [10], the presence of meniscus [11], the mesophase type [12], or a change in the film thickness in the course of vibrational motion [13]. For example, it was shown in [3] that the film inhomogeneity caused by the presence of a meniscus involved in the vibrations cardinally alters the spectral characteristics of the film. Given the possible asymmetry of the meniscus shape (*7* in Fig. 1), one can naturally explain the appearance of nonlinearity responsible for the asymmetry of the elastic properties of a freely suspended film. In this case, from purely geometrical considerations it follows that, in the presence of the transition region (meniscus), the film-area increment may be different for the film motions up and down. This will give rise to different surface-tension increments upon film deformation and, hence, to the appearance of asymmetry in the action of the restoring reactive force.

Note in conclusion that we have demonstrated the two-frequency mixing effect in a nonlinear mechanical system representing a plane ferroelectric liquid-crystal film. This effect can be useful in parametric frequency conversion in visible and infrared detectors (Golay cells [14–18]), in which liquid-crystal membranes can be used as the sensitive element of an optical microphone [3]. The frequency upshift will allow the Golay-cell readout speed to be increased and the low-frequency noise to be suppressed.

We are grateful to S.P. Palto for discussions. This work was supported by the Grant-in-Aid for Scientific Research from the Ministry of Education, Science, Sports, and Culture (Japan).

REFERENCES

1. A. Yariv, *Introduction to Optical Electronics* (Holt, Rinehart, and Winston, New York, 1971), Chap. 8.
2. Ş. V. Yablonskiĭ, A. S. Mikhaĭlov, K. Nakano, *et al.*, Zh. Éksp. Teor. Fiz. **120**, 109 (2001) [JETP **93**, 94 (2001)].
3. Serguei V. Yablonskii, Kazuyuki Nakano, *et al.*, Jpn. J. Appl. Phys. (2003) (in press).
4. Sadahito Uto, Eisuke Tazoh, Masanori Ozaki, and Katsumi Yoshino, J. Appl. Phys. **82**, 2791 (1997).
5. P. M. Morse, *Vibration and Sound* (McGraw-Hill, New York, 1936), p. 142.
6. L. D. Landau and E. M. Lifshitz, *Course of Theoretical Physics*, Vol. 6: *Fluid Mechanics*, 3rd ed. (Nauka, Moscow, 1986; Pergamon Press, Oxford, 1987).
7. P. Pieranski, L. Beliard, J.-Ph. Tournellec, *et al.*, Physica A (Amsterdam) **194**, 364 (1993).
8. A. Jakli, L. Bata, A. Buka, and N. Eber, Ferroelectrics **69**, 153 (1986).
9. M. A. Isakovich, *General Acoustics* (Nauka, Moscow, 1973), p. 422.
10. I. Kraus, Ch. Bahr, I. V. Chikina, and P. Pieranski, Phys. Rev. E **58**, 610 (1998).
11. M. Brazovskaya, H. Dumoulin, and P. Pieranski, Phys. Rev. Lett. **76**, 1655 (1996).
12. P. E. Cladis, P. L. Finn, and H. R. Brand, Phys. Rev. Lett. **75**, 1518 (1995).
13. A. Boudaoud, Y. Couder, and M. B. Amar, Phys. Rev. Lett. **82**, 3847 (1999).
14. G. Chol, Y. Marfaing, M. Munsch, P. Thorel, and P. Combette, *Les Detécteurs de Rayonnement Infra-Rouge* (Dunod, Paris, 1966; Mir, Moscow, 1969).
15. M. J. Golay, Rev. Sci. Instrum. **18**, 357 (1947).
16. Circuit for Automatic Tunneling-Controlled Golay Cell, NPO-20035-1; NASA Tech. Brief **23** (4), 33 (1999).
17. A. H. Lumpkin, N. S. Sereno, and D. W. Rule, in *The Book of Abstracts of 22nd International Free Electron Laser Conference and 7th FEL Users Workshop, Durham, North Carolina, USA* (2000), MO-4-10.
18. G. A. Krafft, P. Piot, K. Jordan, and J. Song, in *Proceedings of Sixth European Particle Accelerator Conference, EPAC'98, Stockholm* (1998), p. 1580.

Translated by V. Sakun

JETP Letters, Vol. 77, No. 3, 2003, pp. 143–145. Translated from Pis'ma v Zhurnal Éksperimental'noĭ i Teoreticheskoĭ Fiziki, Vol. 77, No. 3, 2003, pp. 171–174.

Raman Scattering in Multilayer Structures with CdTe Quantum Dots in ZnTe

L. K. Vodop'yanov[1, *], V. S. Vinogradov[1], N. N. Mel'nik[1], and G. Karczewski[2]

[1] *Lebedev Physical Institute, Russian Academy of Sciences, Moscow, 119991 Russia*

**e-mail: vodopian@sci.lebedev.ru*

[2] *Institute of Physics, Polish Academy of Sciences, 02-668 Warsaw, Poland*

Received December 27, 2002

Raman spectra in superlattices composed of layers of self-assembled CdTe quantum dots separated by ZnTe barriers are investigated. As the barrier thickness increases, a high-frequency shift of all peaks is observed, which is explained by a decrease in the lattice constant averaged over the volume of the entire structure. Peaks are found at a CdTe TO mode frequency of 140 cm^{-1} and also at 120 cm^{-1}. The first peak is assigned to the symmetric Coulomb (interface) mode of the quantum dot material, and the low-frequency peak is assigned to the symmetric mode of the phonons captured in the quantum dot. This combination of modes in structures with quantum dots has not been observed previously. © *2003 MAIK "Nauka/Interperiodica".*

PACS numbers: 78.67.Pt; 78.67.Hc; 78.30.Fs

Great interest has been observed recently in studying the properties of layers of semiconductor materials with a mismatch between their lattice parameters. Favorable conditions for the formation of self-assembled quantum dots (QDs) are created in such layers. Considerable attention is given to studying QDs in structures based on Ge/Si and III–V compounds (InAs/GaAs, InSb/GaSb, etc.). The physical properties of QDs in structures based on II–VI compound semiconductors are relatively less understood. Quantum dots in II–VI structures were found in [1] by analyzing photoluminescence spectra. Multilayer structures with selenide-based QDs were comprehensively studied in [2–4], where spatial correlation was found between QDs contained in two consecutive layers. Layers with telluride-based QDs were studied in [5, 6]. It was found that the occurrence of correlations between QDs contained in adjacent layers depends on the thickness of the ZnTe barriers separating the layers with CdTe quantum dots. However, the works mentioned above are devoted to studying the structural and electronic (photoluminescence) properties of QD structures. The lattice dynamics of QD structures are less understood. Meanwhile, an analysis of vibrational spectra gives a wealth of information on the physical properties of these structures, in particular, on elastic stresses, QD shape, phonon dispersion, etc.

Vibrational excitations in CdS and CdSe nanocrystals embedded in a glass matrix were studied experimentally and theoretically in [7–9]. Peaks at the frequencies of CdS and CdSe LO phonons and their long-wavelength satellites assigned to interface phonons were observed in Raman spectra. The Raman spectra of CdSe QD layers in ZnSe were studied in [10], and a different picture was observed. An interface phonon peak and a CdSe LO phonon band were seen on the low-frequency side of the ZnSe LO phonon band. Thus, the Raman spectra of different structures with QDs are qualitatively different. This is the reason why it was of interest to investigate the Raman spectra of a structure composed of several layers of CdTe QDs separated by ZnTe barriers of different thickness. Manifestations of elastic stresses varying with the ZnTe barrier thickness were revealed in the spectra. However, the most interesting result was in finding new Raman peaks that previously had been observed neither in bulk materials constituting the structure nor in other structures with QDs. These peaks will be explained below.

Superlattices were grown by molecular-beam epitaxy on a GaAs(100) substrate. A CdTe buffer layer 4.5 μm thick was deposited on the substrate. Next, a superlattice composed of 200 periods of CdTe layers was grown on the buffer layer. The CdTe layers were 2.5 monolayers (ML) thick and separated by ZnTe barriers with a thickness changing from 15 to 75 ML. The structures grown were investigated on a JEOL 2000 transmission electron microscope (TEM) with a point resolution of 0.27 nm. An analysis of the variations of the lattice parameter in the growth direction showed that CdTe islands with a diameter of 6–10 nm and a thickness of about 2 nm were observed in the structures studied. The TEM images revealed that vertical correlation existed between CdTe islands for a certain minimal barrier thickness (25 ML). This correlation manifested itself in the fact that the next island was located over the lower one, but at an angle of 40° to the growth direction. The observed vertical correlation of QDs is

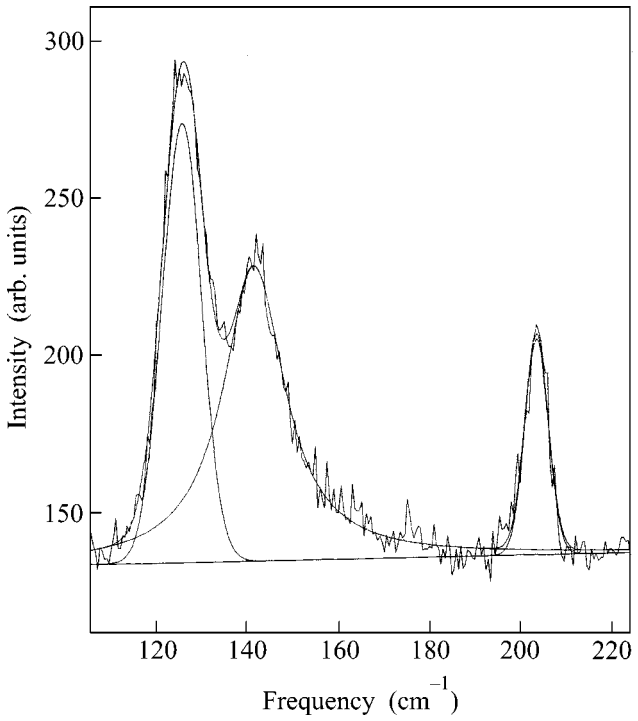

Fig. 1. Raman spectra measured for a B25 superlattice (the barrier width is 25 ML) at room temperature in the backscattering geometry upon excitation by the 4880 Å line of an argon laser. Curves with noise represent the experimental spectrum, and smooth curves are the result of contour analysis.

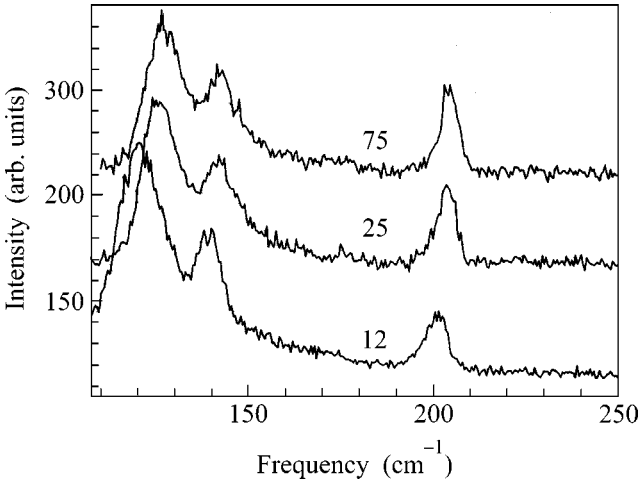

Fig. 2. Raman spectra for three superlattices with various widths of the potential barrier: 12, 25, and 75 ML. The experimental conditions are the same as in Fig. 1.

explained by the elastic anisotropy of the (ZnTe) matrix material [5, 6].

The Raman spectra were measured on a U-1000 spectrometer in the backscattering geometry upon excitation by various lines of an Ar^{2+} laser. The spectral resolution was 1 cm^{-1}.

A typical Raman spectrum measured at room temperature for a B25 superlattice with a ZnTe barrier width of 25 ML, a QD layer thickness of 2.5 ML, and the number of periods $N = 200$ is presented in Fig. 1. The Ar laser line at 4880 Å was used as the exciting line. In order to decrease the background level of scattered light, the exciting laser beam was directed at an angle of 40° to the structure surface. The scattered light was analyzed in the structure-growth direction (z direction) with sample axes $x \parallel [100]$, $y \parallel [010]$, and $z \parallel [001]$. According to the selection rules, only scattering by longitudinal optical phonons is allowed for this configuration. Three Raman peaks are observed in the spectrum presented in Fig. 1. The high-frequency peak at 201 cm^{-1} is evidently related to the LO mode of ZnTe, but with the frequency shifted by 2 cm^{-1} to lower energies. For an unperturbed ZnTe crystal, the LO mode has a frequency of 203 cm^{-1}. The two other observed Raman peaks fall in the region of CdTe vibrational excitations. However, it is immediately evident that the Raman peak corresponding to the LO mode of CdTe at 171 cm^{-1} is absent. The peak at 139 cm^{-1} appeared in the spectrum, is close to the CdTe TO mode (140 cm^{-1}), but it is active in the Raman spectrum. The intense low-frequency peak at 126 cm^{-1} appears to be rather unusual for structures based on II–VI compounds. It should be noted that the observed Raman spectrum has a resonance character. Thus, the spectrum of the same B25 sample measured upon excitation by the 5145-Å line reproduces the main features of the spectrum obtained at 4880 Å but has a considerably lower intensity.

Three spectra measured upon excitation by the 4880-Å line for superlattices differing in the widths of the separating ZnTe barriers (12, 25, and 75 ML) are shown in Fig. 2. It is evident that all observed Raman peaks are shifted to lower energies as the width of the potential barrier increases. This is explained by a decrease in the lattice constant averaged over the volume of the entire structure.

Using a computer program of the decomposition of Raman peaks into contours (Fig. 1), we obtained accurate values of the parameters for each peak: its position in the frequency scale, intensity, and full width at half height (FWHH). It should be noted that the low-frequency peak at ~120 cm^{-1} is approximated well by a Gaussian curve, whereas the neighboring higher frequency peak at ~140 cm^{-1} has a Lorentzian shape.

Let us discuss the nature of these peaks. We tried to interpret these peaks using the theory developed in [7–9], but failed. Therefore, we reanalyzed the problem. In order to describe the vibrational modes of the lattice in a uniform way in the region of small and large wave vectors $\mathbf{k}$, the spatial dispersion of the permittivity should be taken into account. We will do that in the simplest form

$$\varepsilon(\omega, \mathbf{k}) = \varepsilon_\infty + (\varepsilon_0 - \varepsilon_\infty)/[1 - (\omega/\omega_0(\mathbf{k}))^2], \qquad (1)$$

where $\omega_0(\mathbf{k})^2 = \omega_0^2[1 - \gamma(ak)^2]$; ε_0 and ε_∞ are the low-frequency and high-frequency dielectric constants, respectively; ω_0 is the TO phonon frequency at the center of the Brillouin zone ($\mathbf{k} = 0$); a is the lattice constant; and γ is a constant characterizing dispersion. The spectrum of vibrational excitations in a homogeneous substance is described by the relation $\omega^2\varepsilon(\omega, \mathbf{k}) = (ck)^2$. Let us solve this equation with respect to k^2 and pass to the limit $c \longrightarrow \infty$ (neglecting retardation). We will obtain two solutions $k^2 = 0$ and $k^2 = q^2$, where $q^2 = [1 - (\omega/\omega_0)^2]/a^2\gamma$. In order to solve the nonuniform problem of a QD, which we represent as a sphere of radius R, the change $k^2 \longrightarrow -\Delta$ should be made. Then, we will obtain the Laplace equation $\Delta\varphi = 0$ for the long-wavelength (Coulomb) modes and the wave equation $(\Delta + q^2)\varphi = 0$ for the short-wavelength ("mechanical") modes, where φ is the (quasi)electrostatic potential. Then, the problem is solved in the standard way. The continuity of the potential and the induction at the sphere boundary is required for the longitudinal modes, and the continuity of the potential and the transverse components of the electric field is required for the transverse modes. The latter case will not concern us, because it leads to torsional modes, which are not active in Raman spectra. In order to solve the problem of longitudinal modes, the potential is expanded in spherical functions Y_{Lm}. The radial part of the potential in the case of Coulomb modes is described by the functions r^L inside and $r^{-(L+1)}$ outside the sphere; in the case of mechanical modes, it is described by the spherical Bessel functions $j_L(z)$ inside and by the $h_L^2(z)$ or $(\pi/2z)^{1/2}K_{L+1/2}(z)$ functions outside the sphere [11]. For the Coulomb modes, the boundary conditions lead to the following dispersion relation:

$$\varepsilon_i(0, \omega)L = \varepsilon_e(0, \omega)(L + 1), \qquad (2)$$

where indices i and e designate, respectively, the parameters of the material inside and outside the sphere. The modes with the angular momentum $L = 0$ make the greatest contribution. In this case, Eq. (2) has the following solutions: the first one, when $\varepsilon_i(0, \omega) = \infty$, $\omega = \omega_{0i} \equiv \omega_{\mathrm{TO}}(\mathrm{CdTe})$; and the second one, when $\varepsilon_e(0, \omega) = 0$, $\omega = \omega_{\mathrm{LO}}(\mathrm{ZnTe})$. Thus, though the $\omega = \omega_{0i}$ mode is longitudinal, its frequency coincides with the frequency of transverse vibrations inside the sphere. This occurs because the symmetric charge at the surface of the sphere induced by vibrations does not create (according to the Gauss theorem) an electric field inside it. On the other hand, this charge affects the vibrations of the material outside the sphere, which leads to the appearance of the mode with the frequency of the LO vibrations. The aforesaid is also true for a spheroid. Note that both these modes were ignored in the theoretical consideration given in [7–9]. For the longitudinal mechanical modes, in the case of a significant frequency separation between the optical modes of the materials inside and outside the sphere, the boundary condition leads to the equation

$$j_L(q_iR) = 0. \qquad (3)$$

This relation describes the quantization of the phonons captured in the QD. It was obtained in [7, 8]. However, it had a different meaning there, because it was assigned to the band of longitudinal vibrations.

Identifying the peak observed at 140 cm^{-1} with the symmetric mode $\omega = \omega_{0i}$ and the peak at 120 cm^{-1} with the captured phonon, we can estimate the parameter γ_i. Assuming that $L = 0$ in Eq. (3), we obtain $1 - (\omega/\omega_{0i})^2 = \gamma_i(n\pi a_i/R)^2$ ($n \neq 0$). Setting in this relation $\omega_{0i} = 140$ cm^{-1}, $\omega = 120$ cm^{-1}, $n = 1$, $a_i = 6.481$ Å, $R = (w^2h)^{1/3}$, $w = 30$–50 Å, and $h = 10$ Å (QD halfwidth and halfheight), we obtain $\gamma_i = 0.28$–0.55.

As to the symmetric mode of the quantum dot $\omega = \omega_{\mathrm{LO}}(\mathrm{ZnTe})$, its peak is apparently superposed on the peak of the dipole mode with the same frequency $\omega = 200$ cm^{-1} and is not resolved in this experiment. Apparently, it is observed in CdSe/ZnSe [10].

Thus, vibrational modes with frequencies of 140 and 120 cm^{-1} were observed in this work in superlattices with CdTe/ZnTe quantum dots. The first of them was identified with the symmetric Coulomb (interface) mode of the QD material (CdTe), and the second (with a frequency of 120 cm^{-1}), with the symmetric mode of the phonons captured in the QD.

This work was supported by the Russian Foundation for Basic Research, project no. 03-02-7110.

REFERENCES

1. V. S. Bagaev, V. V. Zaitsev, V. V. Kalinin, *et al.*, Solid State Commun. **88**, 777 (1993).
2. L. Krestnikov, M. Strassburg, M. Caesar, *et al.*, Phys. Rev. B **60**, 8695 (1999).
3. N. Peranio, A. Rosenauer, D. Gertsen, *et al.*, Phys. Rev. B **61**, 16015 (2000).
4. D. Litvinov, A. Rosenauer, D. Gertsen, *et al.*, Phys. Rev. B **61**, 16819 (2000).
5. G. Karczewski, S. Mackowski, M. Kutrowski, *et al.*, Appl. Phys. Lett. **74**, 3011 (1999).
6. S. Mackowski, G. Karczewski, T. Wojtowicz, *et al.*, Appl. Phys. Lett. **78**, 3884 (2001).
7. M. P. Chamberlain, C. Trallero-Giner, and M. Cardona, Phys. Rev. B **51**, 1680 (1995).
8. C. Trallero-Giner, A. Debernardi, and M. Cardona, Phys. Rev. B **57**, 4664 (1998).
9. F. Comas, C. Trallero-Giner, N. Studart, *et al.*, Phys. Rev. B **65**, 073303 (2002).
10. H. Rho, H. E. Jackson, S. Lee, *et al.*, Phys. Rev. B **61**, 15641 (2000).
11. *Handbook of Mathematical Functions*, Ed. by M. Abramowitz and I. A. Stegun (National Bureau of Standards, Washington, 1964; Nauka, Moscow, 1979).

Translated by A. Bagatur'yants

JETP Letters, Vol. 77, No. 3, 2003, pp. 146–149. Translated from Pis'ma v Zhurnal Éksperimental'noĭ i Teoreticheskoĭ Fiziki, Vol. 77, No. 3, 2003, pp. 175–178.

Nonstationary Effects in Nitrogen Multipulsed Nuclear Quadrupole Resonance

V. T. Mikhal'tsevich* and T. N. Rudakov

Thorlock International Ltd., Cannington 6107, WA, Australia

**e-mail: vasily@qrsciences.com*

Received January 9, 2003

Multiple echoes in the envelope of the nuclear quadrupole resonance (NQR) signal were obtained in a field of multipulse sequences in powdered nitrogen-containing materials at room temperature. Echo signals were observed over a wide range of pulse rotation angles. It is shown that an analogue of the magic NMR echo can be obtained in the field of multipulse sequence. © *2003 MAIK "Nauka/Interperiodica"*.

PACS numbers: 76.60.Gv

The experimental observation of nonstationary phenomena in the effective field of multipulse sequences in ^{14}N nuclear quadrupole resonance (NQR) was reported in [1–5]. The experiments described in the cited works were carried out for $NaNO_2$ samples at the exact resonance with the transition frequency $\nu_+ = 4.93125$ MHz and a temperature of 77 K for the sequences

$$(\varphi_0)_x - (\tau - \varphi_y - 2\tau - \varphi_{-y} - \tau)_n - [(\tau - \varphi_{-y} - 2\tau - \varphi_y - \tau)_{2n} - (\tau - \varphi_y - 2\tau - \varphi_{-y} - \tau)_{2n}]_N, \quad (1)$$

and

$$(\varphi_0)_x - (\tau - \varphi_y - 2\tau - \varphi_{-y} - \tau)_n - [(\varphi_1)_{-y} - (\tau - \varphi_y - 2\tau - \varphi_{-y} - \tau)_{2n}]_N, \quad (2)$$

where φ_0 is either $\pi/2$ or 0 and $\varphi = \varphi_1 = \pi$. In all cases, the signal was detected at the end of each two-pulse cycle.

The observed effects manifest themselves in the appearance of induction and echo in the envelope of the NQR signals, with the number of echoes coinciding with the number N of supercycles in the sequence.

In this communication, we report experimental evidence for the general character of the effects discovered in [1–5]. We obtained multiple echo signals in a number of powdered substances with substantially different relaxational constants and electric-field gradient (EFG) asymmetry parameters η at room temperature (20°C), in particular, at the $\nu_+ = 4.604$ MHz line in sodium nitrite $NaNO_2$ (Fig. 1a), at $\nu_+ = 5.302$ MHz in octogene $C_4H_8N_8O_8$ (Fig. 1b), and at a frequency of 3.308 MHz in hexamethylenetetramine $C_6H_{12}N_4$ (Fig. 1c). Signals were recorded using pulse sequences of the form (1) or (2) after accumulating 200 pulses with the rotation angles φ_0, φ, and φ_1 varying in a broad range of their values. An example of the NQR envelope as a function of the rotation angle φ is shown in Fig. 2 for the sequence (2) with $\varphi_1 = 1.32\pi$ (doubled 90° pulse in a powder) at the ν_+ transition in $NaNO_2$.

All experiments were accomplished on a spectrometer equipped with an "Apollo" console (Tecmag), a power amplifier (Electronic Navigation Industries, model A-150), a Miteq AU-2A-0150-BNC preamplifier, and a homemode probe in the form of a parallel resonance circuit with a quality factor of ~200. The mass of each sample was 60 g.

To separate signal components corresponding only to the preparatory pulse, the phases of the prepulse and of the detector reference voltage were reversed at each repetition of the multipulse sequence. In this scheme, all free-induction and echo-signal components generated by sequence pulses other than the prepulse are subtracted, while the echo signals related to the prepulse are summed. The sequence repetition time was $5T_1$, where T_1 is the spin-lattice relaxation time. The signal detection time at the end of each cycle was 128 μs.

We briefly consider these effects theoretically by the example of a nitrogen-containing single-crystal sample with $\eta \neq 0$ subjected to the simplified sequence (2)

$$(\varphi_0)_x - (\tau - \varphi_y - 2\tau - \varphi_{-y} - \tau)_{n_1} - (\varphi_1)_{-y} - (\tau - \varphi_{-y} - 2\tau - \varphi_y - \tau)_{n_2} \quad (3)$$

with pulse rotation angles $\varphi_0 = \pi/2$ and $\varphi = \pi$. We will restrict ourselves to a two-particle model. Let sequence (3) irradiate the resonance transition $\omega_p/2\pi$. In terms of the operator of effective spin 1/2 and two-particle operators, the quadrupole Hamiltonian H_q and its secular part H_d with respect to the Hamiltonian of homonuclear dipole interactions (HDIs) are, respectively [6],

$$H_q \sim \omega_p S_z^p = \omega_p(2K_x^r + L_z + M_z); \quad (4)$$

$$H_d = 2\sum_{k=p,q,r}\Omega_k(S_x^kS_x^k + S_y^kS_y^k)$$
$$\sim \Omega_p K_z^q + (\Omega_q - \Omega_r)(M_z - L_z), \quad (5)$$

where Ω_i are the HDI tensor components; ω_i are the frequencies of three nitrogen nuclear resonance transitions ($i = p, q, r$); and the two-particle operators K_z^q, M_z, and L_z are related to three independent operator subspaces K, L, and M. The operator commutation rules in the L-, and M-operator subspaces are the same and fully coincide with the analogous rules for the standard case of spin $I = 1/2$ [6]. All relationships for the operators K_l^p are identical with those for the operator S_l^p of effective spin 1/2 with the same indices. Taking into account the relations [6] $S_l^p = 2K_x^{\lambda_l} + M_l + L_l$ ($l = x, y, z$; $\lambda_x = p$, $\lambda_y = q$, $\lambda_z = r$), one obtains for the initial density matrix after the action of prepulse φ_0

$$\rho(0) \sim S_y^p = 2K_x^q + L_y + M_y. \quad (6)$$

According to the Waugh theory, the average Hamiltonian approximating the action of one cycle ($\tau - \varphi_y - 2\tau - \varphi_{-y} - \tau$) is [7]

$$H_{av} = \frac{1}{2}(H_d + \tilde{H}_d) \sim \Omega_p(K_z^q\cos^2\varphi - K_y^q\sin\varphi\cos\varphi)$$
$$+ (\Omega_q - \Omega_r)((M_z - L_z)\cos^2(\varphi/2)$$
$$- (M_y - L_y)\sin(\varphi/2)\cos(\varphi/2)), \quad (7)$$

where $\tilde{H}_d = \exp(-i\varphi S_y^p)H_d\exp(i\varphi S_y^p)$.

The action of sequence (3) on the spin system is described by the density matrix of the form ($t_c = 4\tau$)

$$\rho((n_1 + n_2)t_c) = \exp(-in_2t_cH_{av})\exp(iS_y^p\varphi_1)$$
$$\times \exp(-in_1t_cH_{av})\rho(0)\exp(in_1t_cH_{av})\exp(-iS_y^p\varphi_1)$$
$$\times \exp(in_2t_cH_{av}). \quad (8)$$

Setting $\varphi = \pi$, one obtains the following expression for the envelope of NQR signals

$$M \sim \mathrm{Tr}(\rho(n_1t_c), S_x^p + iS_y^p) = \cos(n_1\Omega_pt_c)\cos(n_2\Omega_pt_c)$$
$$- \cos(2\varphi_1)\sin(n_1\Omega_pt_c)\sin(n_2\Omega_pt_c). \quad (9)$$

For $\varphi_1 = \pi$, Eq. (9) coincides with the expression for the signal envelopes observed upon the action of sequence (1) with $\varphi = \pi$.

This result is cardinally different from the results obtained in [5], despite the fact that we used the analogous theoretical approach.

Note also that, for the MW-2 sequence and its modification with $\varphi = \pi$, the contribution from the Hamiltonian of inhomogeneous broadening to the signal is virtually absent, much as this happens with NMR [7].

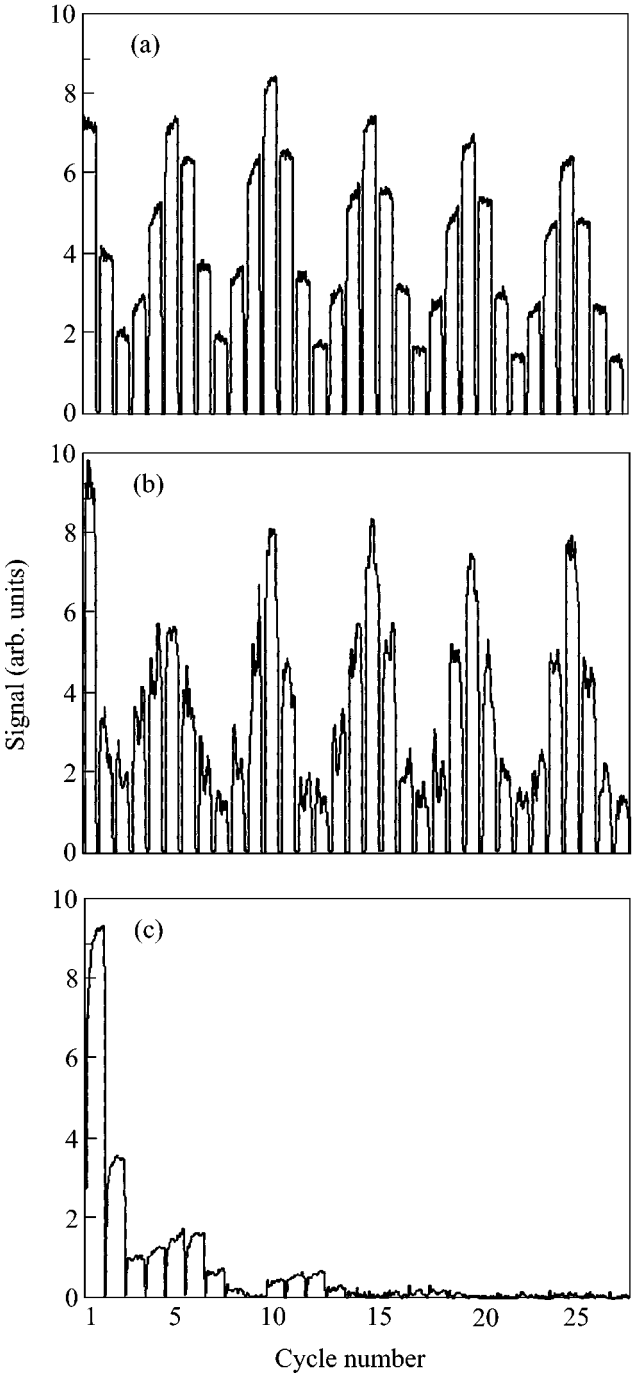

Fig. 1. Induction and echo signals obtained upon the irradiation of powdered substances at 20°C by sequence (2) ($n = 3$, $\varphi_0 = \varphi = 0.66\pi$, $\varphi_1 = 1.32\pi$, $\tau = 128$ μs) with the prepulse phase alternating every repetition. (a) Sodium nitrite $NaNO_2$, ν_+ line, and the number of supercycles $N = 5$. (b) Octogene $C_4H_8N_8O_8$, ν_+ line, and $N = 5$. (c) Hexamethylenetetramine $C_6H_{12}N_4$, resonance transition at 3.308 MHz, and $N = 4$.

Let us consider two particular cases for Eq. (9).

For $\varphi_1 = \pi$, the magnetization of the spin system is

$$M \sim \cos((n_1 + n_2)\Omega_pt_c),$$

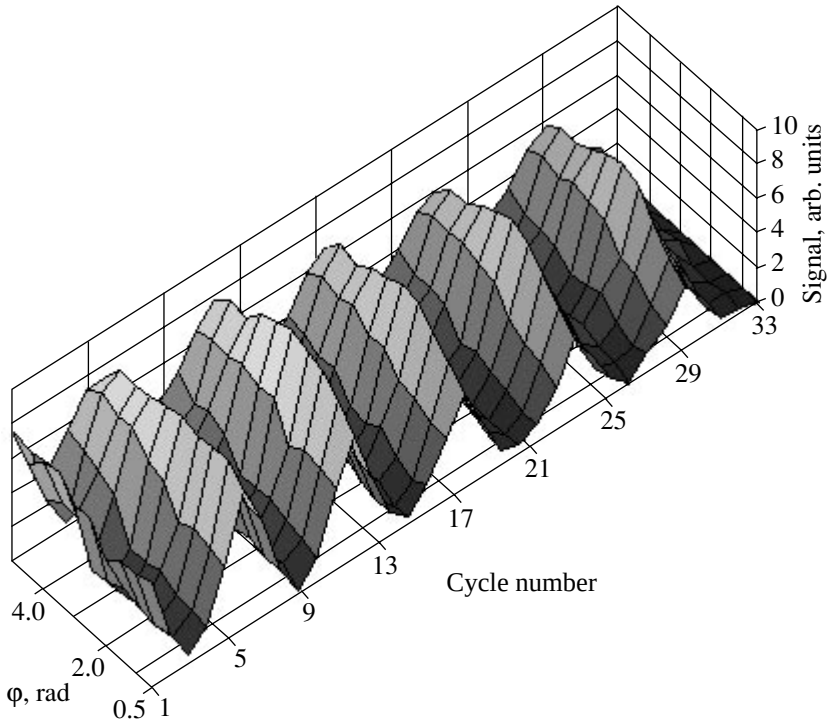

Fig. 2. NQR-signal amplitude for a $NaNO_2$ powder at $\nu_+ = 4.604$ MHz for sequence (2) ($n = 3$, $N = 5$, $\varphi_1 = 2\varphi_0 = 1.32\pi$), as a function of the rotation angle and the cycle number in the sequence.

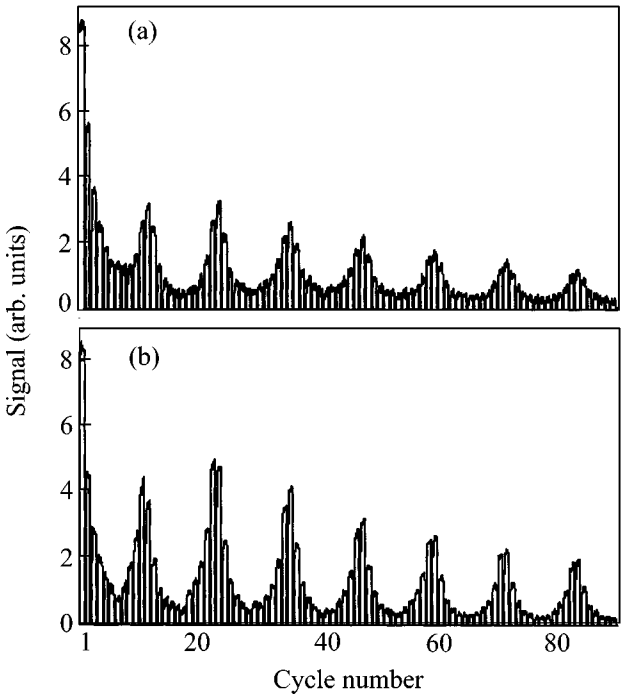

Fig. 3. Induction and echo signals in powdered $NaNO_2$ at 20°C, as obtained upon irradiation by sequence (2) with $n = 6$, $\varphi = 2\varphi_0 = 1.32\pi$, and φ_1 = (a) 1.32π and (b) 0.66π.

and, for $\varphi_1 = \pi/2$,

$$M \sim \cos((n_1 - n_2)\Omega_p t_c).$$

The action of sequence (2) on the powdered $NaNO_2$ is shown in Fig. 3a for $n = 6$ and $\varphi = \varphi_1 = 1.32\pi$ and, in Fig. 3b, for $\varphi = 2\varphi_1 = 1.32\pi$. One can see from these figures that the echo signals in the second case are more than 1.5 times more intense. Since the principal HDI tensor axes in the powder are arbitrarily oriented about the axis of the rf coil, a portion of spins, for which the condition $\Omega_p = \pi/n_1 t_c$ or $\exp(\Omega_p 2n_1 t_c) = 1$ is met with a relatively high accuracy, is also present if $1/t_c \ll \|H_d\|$. These spins produce the signal in the first case. In the second case, the HDI is reversed in each sequence supercycle, so that the condition $\Omega_p = \pi/n_1 t_c$ is not necessary, and the signal is produced by a considerably larger number of spins. The second case can be considered as a certain analogue of magic echo in solid-state NMR [8]. In both examples, the effective decay time for the echo-signal envelope is approximately the same and equal to $T_{2e} = 45$ ms. Note, for comparison, that the spin-lattice relaxation time T_1 for the ν_+ line in a $NaHO_2$ powder is 90 ms at 20°C [9].

Note that the case of $C_6H_{12}N_4$ requires a separate theoretical analysis, because the corresponding asymmetry parameter $\eta = 0$, and hence the above theoretical analysis does not apply in this case.

REFERENCES

1. V. L. Ermakov, R. Kh. Kurbanov, D. Ya. Osokin, *et al.*, Pis'ma Zh. Éksp. Teor. Fiz. **54**, 464 (1991) [JETP Lett. **54**, 466 (1991)].
2. D. Ya. Osokin, V. L. Ermakov, R. Kh. Kurbanov, *et al.*, Z. Naturforsch. A **47**, 439 (1992).
3. D. Ya. Osokin, R. Kh. Kurbanov, and V. A. Shagalov, Pis'ma Zh. Éksp. Teor. Fiz. **62**, 289 (1995) [JETP Lett. **62**, 309 (1995)].
4. D. Ya. Osokin and V. A. Shagalov, Solid State Nucl. Magn. Reson. **10**, 63 (1997).
5. D. Ya. Osokin, Zh. Éksp. Teor. Fiz. **115**, 1580 (1999) [JETP **88**, 868 (1999)].
6. V. L. Ermakov and D. Ya. Osokin, Mol. Phys. **53**, 1335 (1984).
7. M. Mehring and V. A. Weberruβ, *Object-Oriented Magnetic Resonance* (Academic, London, 2001), p. 330.
8. W.-K. Rhim, A. Pines, and J. S. Waugh, Phys. Rev. Lett. **25**, 218 (1970).
9. A. N. Garroway, M. L. Buess, J. P. Yesinowski, *et al.*, Proc. SPIE **2092**, 318 (1993).

Translated by V. Sakun